

The Number Density of Low Surface Brightness Galaxies with $23 < \mu_0 < 25$ V mag/arcsec 2

Julianne J. Dalcanton^{1,2,3}

Observatories of the Carnegie Institution of Washington, 813 Santa Barbara St, Pasadena, CA 91101
&

Princeton University Observatory, Princeton, NJ 08544

David N. Spergel, James E. Gunn⁴

Princeton University Observatory, Princeton, NJ 08544

Maarten Schmidt

Palomar Observatory, California Institute of Technology, Pasadena, CA 91125

Donald P. Schneider⁵

Department of Astronomy & Astrophysics, The Pennsylvania State University, University Park, PA 16802.

ABSTRACT

We present results of a large area CCD survey for low surface brightness galaxies (LSBs) that reaches central surface brightnesses of 25 mag/arcsec 2 in V . We have analyzed 17.5 degree 2 of transit scan data, and identified a statistical subset of 7 pure disk LSB's with central surface brightnesses fainter than $\mu_0 = 23$ V mag/arcsec 2 and with angular exponential scale lengths larger than $\alpha = 2.5''$. The LSB detection is entirely automated, and the selection efficiency of the survey is well-quantified. After correcting for the selection efficiency, we find a surface density of $4.1_{-2.1}^{+2.6}$ galaxies/degree 2 for LSBs in the considered range of μ_0 and α (90% confidence levels), with the largest correction being due to the area lost behind bright stars, and the difficulty in detecting LSBs with small angular sizes.

We have measured redshifts to the final sample of LSBs, and find them to be at distances comparable to those probed by large galaxy catalogs, and to have intrinsic scale lengths of $1.7 - 3.6$ h_{50}^{-1} kpc, also comparable to normal galaxies. We use the redshifts and the selection efficiency to calculate the number density in LSBs with $23 < \mu_0 < 25$ V mag/arcsec 2 and find $\mathcal{N} = 0.01_{-0.005}^{+0.006}$ galaxies h_{50}^3 Mpc $^{-3}$, with 90% confidence. The measurement of the absolute number density of LSBs probably represents a lower limit, due to very strong biases against LSBs with bulges or edge-on LSBs in our sample. Comparing the LSB number density to the number density of normal galaxies with either similar scale lengths or similar luminosities, we find that the number density of LSBs with $23 < \mu_0 < 25$ V mag/arcsec 2 is comparable to or greater than the number density of normal galaxies. The luminosity density in LSBs is comparable to the luminosity density of normal galaxies with similar luminosities, but is a factor

¹e-mail address: jd@ociw.edu

²Hubble Fellow

³Visiting Astronomer, Kitt Peak National Observatory, National Optical Astronomy Observatories, operated by the Association of Universities for Research in Astronomy, Inc., under contract with the National Science Foundation.

⁴Visiting Associate, Palomar Observatory

⁵Guest Investigator, Palomar Observatory

of 3-10 smaller than the luminosity density of normal galaxies with similar scale lengths. The relative LSB number density and luminosity density agree well with the theoretical predictions of Dalcanton et al. (1997). The redshift-space distribution of the LSBs suggests that the trend for low surface brightness galaxies to have weak small-scale correlations may continue to the fainter surface brightnesses covered in this survey.

1. Introduction

During the past twenty years, there has been a developing appreciation of the strong biases against finding galaxies of low surface brightness. These biases arise because the night sky is not particularly dark. Airglow, zodiacal light, and undetected stars and galaxies combine to create a optical background whose surface brightness is as bright as the extrapolated central surface brightnesses of large spiral galaxy disks. With such a bright background, the ability to detect a galaxy depends not only upon the integrated luminosity of the galaxy, but also upon the contrast with which the galaxy stands out above the Poisson fluctuations in the background. A compact, high-surface brightness galaxy might be quite easy to detect, while another galaxy with the same total luminosity but with a much more extended, low-surface brightness structure would be difficult to find.

While astronomers routinely consider the limiting magnitude of their galaxy catalogs, only recently have they begun to consider the ways in which surface brightness selection effects shape existing galaxy catalogs. As an example, Freeman (1970) had initially showed that spiral galaxies share the same central surface brightness, with very little dispersion: $\mu_0 = 21.7 \pm 0.3$ B mag/arcsec 2 . Disney (1976), however, convincingly argued that because of the limiting surface brightness of the sample, one would not expect to have detected galaxies with lower surface brightnesses, and thus that there was no particularly compelling reason to believe that the Freeman law reflected the intrinsic properties of spiral galaxies. While Allen & Shu (1979) later showed that the cutoff at bright surface brightnesses does indeed reflect an actual fall-off in the number of galaxies with increasing surface brightness, they concurred with Disney's appraisal of the possible role of selection biases in shaping the faint end of Freeman's surface brightness distribution. Thus, Disney demonstrated that what was thought to be a general property of disk galaxies could in large part be explained by selection biases against finding low surface brightness galaxies (LSBs).

Disney's paper was the genesis of the modern efforts both toward understanding the role that surface brightness selection effects play in shaping existing galaxy catalogs and toward overcoming those biases in newer surveys. Although Disney's work strongly suggested that selection biases could reproduce the Freeman law, it presupposes that there exists a population of low surface brightness galaxies to be biased against. It may have been that there really were almost no galaxies with central surface brightnesses fainter than 22 mag/arcsec 2 . Over the following years and extending through the present, however, there has been an enormous body of observational work that has conclusively demonstrated the existence of low surface brightness galaxies. Indeed, every time a new survey has been extend to fainter surface brightnesses, new LSBs have been discovered.

Previous surveys which have been sensitive to LSBs have fallen into two basic types: large area photographic surveys and deep, small area CCD surveys. Of the first type, the older, diameter-limited Upsalla General Catalog of Galaxies (UGC) (Nilson 1973) had been the workhorse through most of the 70's and 80's. It has been recently supplemented by a catalog of LSBs selected visually from the Second Palomar Sky Survey using the same selection criteria as the UGC catalog but with deeper plates (Schombert et al.

1992, Schombert & Bothun 1988, herein referred to as the “POSS-II” catalog), and now by the APM LSB survey which selected LSBs automatically and by eye using scanned plates from the APM galaxy survey (Impey et al. 1996). Other deep photographic work has been used to search for LSBs in clusters (Impey et al. 1988, Davies et al. 1988, Irwin et al. 1990, Ferguson & Sandage 1988, Sandage & Binggeli 1984). With the exception of the deeper cluster surveys, the photographic work finds very few galaxies whose peak surface brightness is fainter than $\mu = 24 \text{ mag/arcsec}^2$ in B (corresponding to $\approx 23.5 \text{ mag/arcsec}^2$ in V , using mean colors from de Blok 1995, McGaugh 1994), unless they also have high surface brightness bulges.

The second type of LSB survey, the CCD surveys, have concentrated primarily on identifying LSBs within clusters of galaxies (Turner et al. 1993). Due to their small area, these surveys are restricted to finding galaxies of small angular size, which leads to a large degree of confusion between intrinsically low surface brightness galaxies and either high-redshift normal galaxies which appear to have low surface brightness because of $(1+z)^{-4}$ cosmological dimming, or pairs of barely resolved galaxies. A similar field survey by Schwartzenberg et al (1995) also suffers from the same problems, although to a slightly lesser extent due to a larger angular size cutoff. However, the difficulties in untangling the true surface brightness and angular size distributions are compounded by effects of poor seeing and the large pixel size of these surveys. There has also been a promising recent foray into using CCDs to survey for faint field LSBs through cross-correlating an image with a model galaxy profile (Davies et al. 1994). However, the areas surveyed so far are still too small to do more than to verify the promise of this method.

In spite of the limitations, existing surveys have begun to advance our understanding of the density of the LSB population. They have both proven the existence of LSBs, and provided a rich data set for studying the properties of individual LSBs. They have also begun to yield quantitative results about the size of the LSB population. First, several existing photographic and CCD cluster surveys have been used to estimate the relative number density as a function of surface brightness. McGaugh (1996) has used the selection criteria of the Davies (1990) sample to estimate the relative survey volume as a function of central surface brightness, and shown that the distribution of disk surface brightnesses is very broad. The derived distribution of surface brightnesses cuts off sharply brighter than the Freeman surface brightness value, but falls only slowly with decreasing central surface brightness; by $\mu_0(B) = 23 \text{ mag/arcsec}^2$, the number density drops by only a factor of 2-4, but is statistically consistent with a flat distribution in surface brightness. However, this analysis assumes that the distribution of intrinsic disk scale lengths is independent of surface brightness, which does not seem to be true (i.e. the increase in the maximum scale length with decreasing surface brightness – see de Jong & van der Kruit 1994, for example). Thus, there may be systematic offsets in the accessible survey volume as a function of surface brightness, leading to substantial uncertainties in the relative number density as a function of surface brightness.

More recently, the large APM LSB survey has reconstructed the luminosity function of LSBs with central surface brightnesses of $22 \text{ mag/arcsec}^2 < \mu_0(B) \lesssim 24 \text{ mag/arcsec}^2$, using a detailed quantification of the automated detection algorithm (Sprayberry 1997). The survey has 332 galaxies with redshifts, and has $\sim 20\%$ completeness in redshift identification for galaxies with $\mu_0(B) > 23 \text{ mag/arcsec}^2$. They find that, when compared to the CfA survey luminosity function (Marzke et al 1994) which covers a nearly disjoint surface brightness range, the LSBs in their survey add roughly a third to the known luminosity density in galaxies with $M_B < -13$, and more than double the known luminosity density contributed by known galaxies with Irr/Im morphologies.

In the survey described in this paper, we attempt to combine the best features of previous surveys, and to push observations to lower surface brightnesses than have been previously surveyed in the field. We use CCDs to observe a large area of the sky, obtain extremely accurate flat-fielding through the use of drift

scanning, use completely automated detection to allow for a complete and detailed understanding of the selection biases in the survey, and search for galaxies with large angular sizes to reduce the background confusion and to identify LSBs which are most comparable to well-cataloged normal galaxies in large local surveys. In the following section, §2, we outline the basic strategy of our survey, and discuss how it is optimized for reaching the above goals. In §3 we describe the data we have used, and the data processing and selection criteria in detail. In §4 we discuss the properties of the entire sample of objects detected in the survey, and in §5 we focus our attention on the properties of the subset of LSB galaxies. Finally, in §6 we use the LSB subsample to measure the surface density, number density, and luminosity density of LSB galaxies, and compare to the population to normal galaxies. We discuss our estimation of errors in Appendix A. In Appendix B is a general discussion of reconstructing the number and luminosity density of angular diameter limited samples from the observed surface density. We use $H_0 = 50 \text{ km/s/Mpc}$ throughout.

2. Strategy

There are two essential elements to the survey which we have carried out, namely the use of time-delay-and-integrate (TDI) observations to achieve extremely accurate flat-fielding over large areas and the use of optimal smoothing filters to enhance the detection of large LSBs. In a TDI scan (also known as “strip”, “drift”, or “transit” scanning), the telescope is held fixed, while the sky drifts across the field of view of the CCD camera, while lines of charge are stepped from row to row of the CCD to keep track with the sky. Drift scanning averages out the flat-fielding variations along the columns of the chip, and means that each line of the resulting strip of data has the same flat-fielding (or “flat-lining”) characteristics, up to the temporal stability of the chip response. Millions of lines of the data can be combined to create an extremely accurate one-dimensional sky flat for the entire data set, much in the same manner that shift-and-stare techniques can be used to make two-dimensional sky flats. Drift-scanning therefore provides an extremely efficient way of using CCDs to observe large areas of the sky while providing excellent flat fielding.

With the advantage of extremely accurate large scale flat fielding, we can smooth the data over large scales to reveal low surface brightness galaxies which are typically at the limits of detectability, due to Poisson pixel-to-pixel fluctuations in the sky level. To increase sensitivity to galaxies whose surface brightnesses are comparable to the sky brightness, the pixel-to-pixel noise can also be reduced by averaging together many pixels, increasing the effective area of the pixels. While this decrease in noise may be achieved by observing with large CCD pixels or by binning down the charge on the chip, it may also be reached by smoothing high resolution data.

There are several advantages to using smoothing to reduce the pixel-to-pixel noise. First, the smoothing may be done with a filter that is matched to the shape and size of the galaxy for which one is looking; this produces the maximum gain in signal-to-noise for the targeted galaxies. Second, because the original, high-resolution data still exists after smoothing, no information is really lost; the original data can provide additional information about the sources of any low-surface brightness features detected after smoothing. If the smoothing were to have been done by binning the CCD during readout, and not during post-processing, the increase in signal-to-noise would have been optimized for square galaxies, not realistic ones, and most importantly, there would be much more confusion about the source of any fluctuations. Finally, because smoothing allows any filter to be used, one data set may potentially be used to independently survey for galaxies of many different shapes and angular sizes. To avoid contributions from bright foreground objects, we have cleaned images of bright foreground objects, such that subsequent smoothing truly recovers large scale fluctuations in the optical background.

Because the known population of LSBs seems to be well fit by exponential disks (de Jong 1996, de Blok et al 1995, McGaugh & Bothun 1994, Knezeck 1993), we have chosen to use an exponential profile as the filter kernel. We have smoothed with an exponential filter of scale length $5''$, which drops the level of fluctuations by over a factor of ten, a gain that would only have been achieved with over a hundred-fold increase in exposure time. By choosing such a large scale length, we eliminate any confusion between low surface brightness galaxies and distant, cosmologically-dimmed high surface brightness galaxies. For example, galaxies with an apparent scale length of $\approx 5''$ are likely to be within 200 Mpc ($z = 0.03$, assuming an intrinsic scale length of $5 h_{50}$ kpc) and are near enough that $(1 + z)^4$ surface brightness dimming is negligible. This choice of scale length also identifies LSBs within a volume comparable to that which is occupied by NGC and UGC galaxies; a normal galaxy with a $5''$ exponential scale length has an angular diameter of close to $1'$ (assuming $\mu_0 = 21.5$ mag/arcsec 2 and $\mu_{lim} = 26.5$), similar to the angular diameter limit of large photographic surveys.

To identify candidate LSBs, we identify all large regions of connected pixels in the smoothed image which are significantly above the level of the remaining fluctuations in the sky. The entire process – cleaning, smoothing, and searching – is entirely automated, and is repeated with artificial galaxies added to the data to allow a thorough investigation of the selection biases of the survey. We then visually inspect all candidates to identify the subset which are LSBs. We perform additional artificial galaxy tests to test the limits of our ability to classify LSBs. We use these limits to further restrict the LSB subset to the region where our detection and classification efficiencies are well-determined. Finally, we measure redshifts for the final LSB subset, allowing us to measure the absolute number density of the LSBs.

3. Data Processing

3.1. Imaging Data

The survey utilizes existing imaging data, originally taken for the Palomar Transit Grism Survey (Schneider, Schmidt, & Gunn 1994; hereafter SSG) for high redshift quasars. We will give a brief summary of the initial data processing of this data set; see SSG for a detailed description of the survey. The data were taken with the 4-Shooter camera (Gunn et al. 1987) at the Cassegrain focus of the Palomar 200-inch telescope. The 4-Shooter detector consists of 4 800x800 Texas Instrument CCDs, arranged in a 2x2 grid, with a pixel scale of $0.335''/\text{pixel}$. The telescope was operated in transit mode, holding the telescope fixed and allowing the sky to drift across the CCDs while the CCD was clocked to keep pace with the passage of the sky. The drift scan produces four very long images at a fixed declination covering a wide range in right ascension, each strip corresponding to one of the four chips. The strip is cut into 400x1600 images with 120 rows of overlap between adjacent images. Because of difficulties with the high data flow rate, the CCDs were double-clocked and the columns rebinned by a factor of 2, to increase the effect of pixel scale to $0.67''/\text{pixel}$. The seeing was $1.5 - 3''$. The two leading CCDs used the $F555W$ “wide V ” filter, while the two trailing CCDs used $F785LP$ (Griffiths 1990). Following Postman et al. (1996), we will use the shorthand notation of V_4 and I_4 for the combination of the HST filters and the 4-shooter response function. Only the V_4 strips were used, because of the greater susceptibility of the I_4 band to fringing and to low level fluctuations in the sky brightness.

We specifically use the QR and MN strips from the SSG survey, observed in April 1987 and 1988, respectively. (The two-letter notation reflects the fact that each strip is actually composed of two separate strips, corresponding to the two halves of the 4-shooter’s CCD array. We analyze each of the four substrips

(M, N, Q, & R) independently.) The QR strip is at a declination of $\delta = +47^\circ 34' 47''$, and extends from $8^\text{h} - 17^\text{h}$ in right ascension. The MN strip is at a declination of $\delta = +46^\circ 22' 40''$, and extends from $9^\text{h} - 17^\text{h}$ in right ascension.

As described in more detail in SSG, a single bias level, measured in the overscan region, was subtracted from each image. Following this, the lines of all of the images were combined to create a sky-flat for the CCD. The flat did not change significantly over the course of three years. After each image was flattened, a cubic polynomial was fit to the median sky level along the scanning direction and then subtracted to remove any large temporal fluctuations in the image. Further corrections of the temporal variations are described in §3.3. Finally, the two substrips were calibrated against each other by requiring the same mean sky level in each pair of adjacent images. Each image was further overscan corrected by using a five piece cubic spline fit to the overscan region. Following this, the images were trimmed to remove the bias strip, leaving 372x1598 images.

The imaging data were not taken in perfectly photometric conditions, and were initially not photometrically calibrated. However, strip scans allow one to easily detect the presence of cirrus. First, because the strip is a scan both in time and in right ascension, any temporal variations due to the presence of cirrus is easily recognized as structured banding within an individual image, due to the fluctuating brightness of the sky produced by the changing degree of reflection of the light from San Diego. Second, the passage of cirrus dramatically drops the number of objects seen in a given image. Based upon the number counts of Postman et al. (1996) using the identical observational system, if the depth were to change by 1 magnitude, the number of detected objects would change by a factor 3. In contrast, in the data which we used, the number of objects never varies by more than 25% (either RMS or systematically), suggesting that the depth never varies by more than 0.3 magnitudes. In fact, the variation in the depth is certainly even smaller, given that half of the fluctuation amplitude is due to simple Poisson counting, and that there are additional fluctuations in the area lost to bright foreground stars. Using the constancy of the sky brightness and of the number of objects per field as a measure of atmospheric clarity, we have restricted the data to the portions of the night which are most likely to be photometric. When reduced to the most photometric portions of the night, the QR substrips consist of 179 400x1600 images in each band between $8^\text{h} - 13^\text{h}$. The MN substrips consist of 283 400x1600 images in each band. Twenty-eight of the MN images near 11^h are unusable due to the passage of clouds. A total of 868 images were used in the survey. The total area covered by the 4 individual strips is 17.5 degree².

As a test of our judgement, and as a means to calibrate the zero point of the Palomar data, we have taken calibration images of many fields within the strip, under photometric conditions, and find no significant variation in the zero point of the strip scan data in the portions of the night to which we have restricted the data. We have calculated the zero points for the MN and QR strips using calibration data taken in Johnson *V* with the Kitt Peak 0.9m telescope in March of 1994. The Johnson *V* zero point of the Kitt Peak data was calibrated and airmass corrected using 6 independent observations of 8 different standard stars in two separate Landolt (1992) fields, with an 0.015 magnitude rms in the airmass corrected zero point. For the MN strip, we have Johnson *V* images of 7 different fields throughout the strip, 3 of which were observed more than once. These images were used to calculate *V* band magnitudes for objects which fell in the MN strip. Comparing to the count rate for objects in the SSG data to their *V* magnitudes in the KPNO data, we calculate a Johnson *V* zero point for the MN strip of 29.36 ± 0.04 magnitudes per data number, with no systematic difference between the zero points of the two halves of the strip. We will quote Johnson *V* magnitudes for the remainder of the paper, for ease of comparison to other LSB samples; although the data was taken in *V*₄, the color term to correct from *V*₄ to Johnson *V* is small,

$V - V_4 \approx 0.04 - 0.06$, for $V_4 - I_4 \approx 0.5 - 1$ (Postman et al. 1996). The RMS scatter among the 10 calculated zero points of the SSG data agreed with the expected uncertainty in the mean, based upon the uncertainties in the zero points calculated for the individual fields, which were in turn based upon the RMS scatter in the airmass corrected zero point of the KPNO data and in the zero points calculated for the stars in the KPNO transfer standards. The stability of the zero point throughout the MN strip suggests that the atmosphere was uniformly transparent for the portion of the night which met our criteria for being most photometric. The zero point for the MN strip is also consistent with the conversion used for the Palomar Distant Cluster Survey (Postman et al. 1996), which uses the same instrumental configuration.

For the QR strip, we have only one calibrated field, giving a zero point of 29.17 ± 0.04 magnitudes per data number in Johnson V for the QR strip. However, rather than use a single measurement to calibrate the entire QR strip, we will use the zero point of the MN strip for the QR data as well, and recognize the possibility of an 0.2 magnitude offset between the two data sets. We note that the surface brightnesses probed in this paper are up to 7 mag/arcsec 2 fainter than normal galaxies, and thus an error in the photometric calibration of less than half of a magnitude will do little to change the conclusions. Furthermore, given that the number of detected objects per frame and the sky brightness both vary as smoothly in the QR strip as in the MN strip, we do not anticipate finding field-to-field variations in the QR strip zero point which are significantly greater than those seen in the MN strip.

3.2. Removal of Foreground Objects

Producing a map of the background sky requires the removal of all of the high-surface brightness stars and galaxies which are obstructing the view of the background. To identify the intervening objects, FOCAS was used to identify all regions of connected pixels greater than 4 sigma above the mean sky, with a detected area of greater than six pixels after smoothing with FOCAS's built-in filter (Jarvis & Tyson 1981, Valdes 1982). The number of objects found per unit magnitudes began to deviate from a power law at $V = 22$, suggesting that the FOCAS selection is incomplete beyond this point.

In preparation for cleaning, the region that FOCAS had associated with each object was extended by an amount derived from the object's detected area and magnitude. This ensured that any low-surface brightness halo, due to either seeing or to a slowly falling galaxy profile, was included with the central bright regions. The pixels within the object were replaced with values drawn from the local sky histogram, created by sampling within a buffer around the extended region and clipping at 4 sigma above the local mean. This cleaning procedure preserves the large scale distribution of surface brightness. Objects which have large areas for their magnitude (or low magnitudes for their size) are excluded from cleaning to avoid cleaning any brighter LSBs which FOCAS may have been able to detect without additional processing.

While replacing objects with the local sky histogram proved to be effective for objects fainter than roughly 19th magnitude, cleaning brighter, larger objects, would have invested tremendous amounts of computational time in a region guaranteed to be useless for detecting background objects. Instead, large regions around bright objects were removed from the survey by creating masks for each image, which were used throughout processing. Occasionally, the area of the masked region was sometimes too small to completely block out the halo of the masked object. This problem was most commonly manifested in objects on the edges of images, and very occasionally in highly elongated non-boundary objects such as edge-on galaxies and meteor trails. Cases where the masking was insufficient were easily identified in the final catalog and removed from consideration. The two columns on the left and right edges, and fifteen

and thirty rows on bottom and top edges respectively were masked as well, to eliminate the most common regions of incomplete FOCAS identification from consideration. Roughly 39% of the survey area is lost to the masked regions.

In the final cleaned image, the masked regions were set to the median sky level of the unmasked regions. The mask and the cleaned image were then rebinned by a factor of two to save space.

3.3. Removing Large Scale Variations

In drift scans, there are low amplitude row-to-row fluctuations due to temporal variations in the sky brightness ($28.7 - 28.0 \text{ mag/arcsec}^2$ (2-4 ADU) peak-to-peak, when smoothed on scales of $10''$). These fluctuations are constant across a given row, and vary smoothly from row to row, creating very low level bright and dark “bands” across the strip scan. The efficiency of the survey is compromised by the fluctuations; significant low-surface brightness objects that lie in low points are more likely to be missed, while fainter objects that lie on the high points will be detected more frequently. (Although Monte Carlo simulations can measure the variation in efficiency, they cannot compensate for the lost survey area.) We flatten the overall sky background in each image by: (1) setting the masked regions to zero, (2) taking the mean of each row of the masked image and of the mask itself, (3) smoothing each 1-dimensional profile with a boxcar filter $\approx 2'$ wide (roughly 13 seconds, temporally), (4) dividing the smoothed image profile with the smoothed masked profile, and (5) subtracting the resulting 1-d profile from each column of the original image. This produces a significantly flatter image with a roughly zero sky level.

Correcting for large scale variations reduces the survey’s sensitivity to objects of similar scales. We have not lost much sensitivity in the case of this survey however, as the geometry of the strip makes it unlikely that many objects with scales of $2'$ or larger could be detected in the first place. Because of the difficulty in treating boundaries in any smoothing problem, the flattening tends to become inaccurate at the beginning and ending of the image, and adjacent to regions where the entire width of the image has been masked out. These regions were obvious in the final smoothed image, and were eliminated from consideration to avoid false detections. Occasionally there is residual row-to-row structure left in the image after flattening, on scales smaller than the flattening scale. These are also due to temporal variations on scales smaller than 13s, and are typically fainter than $28.5 \text{ mag/arcsec}^2$.

After removing temporal variations, occasionally there are diagonal structures which cannot be due to temporal variations, at the 28 mag/arcsec^2 level. The most likely sources of this excess structure are halos of stars off the field of view and emission from galactic cirrus. Our current data are not adequate for addressing these questions, but repeated, multi-color transit scan observations of a single region, with small random offsets in declination between scans and a larger FOV, would help to constrain the origin of any residual structure.

3.4. Smoothing and Detection

The cleaned, rebinned, and flattened images produced by the previous steps are remarkably featureless. Any residual flattening inaccuracies are invisible, buried well below the pixel-to-pixel variations in the image. Smoothing the cleaned image reduces the pixel-to-pixel noise dramatically, uncovering low surface brightness features. After replacing the masked regions with the image median, we smooth the image with

a radially symmetric exponential profile ($\propto e^{-r/\alpha}$) with $\alpha = 5''$, which optimizes the signal-to-noise ratio increase for objects with exponential profiles identical in size and shape to the smoothing filter. Smoothing with the $5''$ filter reduces the pixel-to-pixel noise⁶ by roughly a factor of twelve (to $\approx 0.7 - 0.9$ ADU). Smoothing with a larger smoothing length of $10''$ reduced the level of fluctuations by an additional factor of only 1.6, indicating that on the scale of the smoothing kernel (8α) the fluctuations in the images are not random, due to the very low level fluctuations discussed in §flattening. The histogram of pixel values for the $10''$ smoothed images also show deviations from the expected Poisson distribution. Because of this indication of residual structure on $40''$ scales, we chose to use only the single scale length to smooth our data; with a larger field of view and reduced temporal fluctuations and scattering, a larger range of smoothing lengths would be more useful than with this particular data set.

A modified version of FOCAS was used to detect all regions in the smoothed image greater than $\pm 3.5\sigma$ above the image median over an area of 25 pixels, corresponding to 11.2 arcsec 2 . The resulting FOCAS catalog was restricted to eliminate any object touching a boundary (the only negative “dark” objects found were also boundary objects) or whose center was within $1.5r_2 + 10''$ (where r_2 is the intensity weighted second moment radius) of the left or right edges, or within $37''$ of bottom edge or $125''$ of the top edge. The buffer on the upper edges is larger to avoid detecting objects in the overlap region in more than one image. With these selection criteria, 868 objects were detected, giving an average of 1 candidate per each frame. We expect the total catalog to include only one or fewer spurious detections due solely to Poisson fluctuations; this is based upon the number of independent detection areas in the survey, after correcting the survey area for the masked areas and the buffered regions along the edges of the images, and upon the peak height of an exponential profile which is 3.5σ above the mean at a radius of $2''$. The absence of “dark” features and the low Poisson probability of false positives suggests that effectively all of the detected features are due to true enhancements in the the mean sky level (although those may in some cases be due to other than astronomical sources, as discussed below).

4. Properties and Classification of Detected Objects

A single image was created for each candidate object, consisting of three adjacent panels (see Figure 2 for an example). The first panel is taken from the original uncleaned, unprocessed image. The second panel is taken from the cleaned image, and has been expanded by a factor of two to match the angular scale of the first panel. The third panel is taken from the smoothed image in which the object was detected, also adjusted to the same angular size as the other two panels. All three panels are centered on the object. These composite images allow easy browsing of the catalog (with much less stringent disk space requirements than saving all the processed data), and were used to assign a classification to the objects, if possible. Classifications were based entirely upon visual inspection of the images.

The classification was given as combinations of the categories below, based upon the associated criteria. The percentages in the brackets are the percentage of objects that have the category as a possible classification and the percentage of objects that have the category as their only possible classification.

- (l) Low surface brightness galaxy – Exhibits smooth, extended emission in the original image.

⁶The “noise” of an image was measured throughout this survey as 1.4826 times the width of the second quartile of the pixel histogram. This reduces to the standard deviation for a Gaussian distribution. Because objects contribute light to the sky rather than take it away, using the second quartile reduces the impact of foreground objects on the measurement of the width of the pixel histogram.

[4.1%,2.4%]

(c) Cluster – Shows evidence that the low surface brightness emission is associated with several compact clumps, either clearly visible or just below the threshold for detection (see Dalcanton 1996). The classification typically reflects one of three cases, corresponding to clusters at different distances: 1) the light is the low-surface brightness component of a nearby cluster that can be clearly identified by large numbers of galaxies in the field; 2) the emission is centered on a single galaxy with several, barely visible companions, probably corresponding to a CD galaxy of a more distant cluster; 3) the emission is centered on a clump of several faint knots of emission, which are probably the centers of distant cluster galaxies just below the threshold of detection. Objects classified as clusters tend to be near other clumps in the smoothed sky maps. In the case of the low redshift clusters, the correlation is due to detecting pockets of dwarf galaxies and tidal debris throughout the cluster region. In more distant clusters, the correlation is most likely due to the presence of subclustering, or to the high amplitude of the cluster-cluster correlation function. This clustering behavior was clearly seen in the recovery of the $z = 0.8$ cluster MS1054 in Dalcanton (1996), where two or three strong peaks were seen in the smoothed sky background, centered on regions of truly high galaxy concentration. [24.3%,19.9%]

(t) Tidal features – Shows evidence that the low surface brightness emission might be due to interactions between galaxies. Used if the emission lies between two close galaxies or is adjacent to a single galaxy that shows signs of being disturbed, especially if there is no other evidence that the light might come from galaxies below the detection limit. The boundary between this class and the cluster class is not always distinct. [2.0%,1.1%]

(g) Groups of Galaxies – Tight groups of foreground galaxies without extended low surface brightness emission. These probably entered the catalog through contamination of the sky histogram of one galaxy with the bright pixels of an adjacent galaxy. However, they form a potentially interesting subclass, and may actually contain true members of the cluster and tidal classes, and thus are not classified as errors. [5.4%,2.8%]

(?) Uncertainty – Represents uncertainty in the classification.

() Unclassified – No evidence for making a classification. Typically has no strong associated foreground emission, or no compelling reason to group the object with one class over another. [52.3%,52.3%]

(*) Errors – Cases where the object’s inclusion in the catalog was more a product of the processing than the object’s internal properties. These cases include incompletely cleaned or incompletely masked objects, or objects which have only been included because they were superimposed on either a halo from an object off the field of view or on regions of inaccurate flattening in the upper and lower edges of the image. [16.2%,16.2%]

Many of the detected objects have more than one possible classification. This is an unavoidable consequence of the detection procedure. While smoothing the cleaned images increases the signal-to-noise to the point where faint features can be detected, the signal-to-noise of the original image, which is used for classification, remains unchanged. Thus, in many cases there is no unambiguous classification, in spite of a significant detection of an EBL fluctuation. For example, there are cases where the feature in the smoothed image does not correspond to any obvious emission in the foreground image. There are other cases where, although the detected region corresponds to one or more high surface brightness features in the original image, the low-surface brightness component responsible for the detection is too faint for any morphology to be visible which might provide a clue as to the proper classification. Note that because classification

requires more signal-to-noise than detection, classified objects are even less likely to be spurious.

There are many cases where, in spite of reasonable signal-to-noise, the classification is ambiguous. An LSB galaxy with a faint bulge or with several HII regions is possibly similar in appearance to a distant cluster with a faint CD galaxy, or even to a tidally disturbed normal galaxy. Because of this confusion, when we create a final catalog of objects which have LSB as their only possible classification, we are underestimating the true contribution of LSBs. Because of their ambiguous classification, we systematically exclude LSBs with high-surface brightness features (i.e. bulges, resolved stars, HII regions) from our catalog of definite LSBs, leaving us with a “pure disk” subsample of the larger LSB population (e.g. see profiles in Figure 3). This is in contrast to visually selected, angular-diameter limited catalogs of LSBs, such as the POSSII and UGC catalogs; a substantial fraction of the LSBs in these catalogs have strong central bulges (for example, see the profiles in McGaugh & Bothun 1994).

5. The LSB Subsample

For the remainder of the paper, we will concentrate on the 21 objects which were classified as candidate LSBs based upon their optical morphology. Of these, 14 were classified as definite LSBs, and an additional 7 were classified as probable LSBs.

In order to determine the central surface brightness and scale length of the LSB candidates, we fit the 21 LSB candidates interactively with IRAF’s “ellipse” surface brightness photometry package. We then further restricted the LSB subsample to include only the 14 LSB candidates whose extrapolated central surface brightnesses were fainter than 23 mag/arcsec^2 in V (corresponding to roughly $23.5 \text{ mag/arcsec}^2$ in B , using the median LSB color of $B - V \approx 0.5$ from McGaugh & Bothun (1994) and de Blok et al. (1995)); because we did not use any photometric information in the initial classification, galaxies classified as potential LSBs were sometimes not dramatically fainter than the Freeman value, and within the range of surface brightnesses that can be better constrained with the much larger APM survey (Impey et al. 1996, Sprayberry et al. 1997). The remaining sample spans a range in central surface brightness of $23 \text{ mag/arcsec}^2 < \mu_0 < 25 \text{ mag/arcsec}^2$ in V and scale lengths of $2'' < \alpha < 7''$. While the profiles are noisy (particularly at large radii) due to the very low signal-to-noise in the unsmoothed image, they are consistently better fit by exponential surface brightness profiles than by deVaucouleur’s profiles.

We estimated the uncertainty in the measured central surface brightness and exponential scale length by performing the identical ellipse fitting and profile fitting on artificial galaxies with the measured properties of each of the LSBs. For galaxies with $\alpha < 5''$, $\mu_0 - \mu_0(\text{true}) = -0.03 \pm 0.06$, and for galaxies with $\alpha > 5''$, $\mu_0 - \mu_0(\text{true}) = 0.06 \pm 0.06$. For galaxies with $\mu_0 < 23.8 \text{ mag/arcsec}^2$, $[\alpha - \alpha(\text{true})]/\alpha = -0.006 \pm 0.09$, and for $\mu_0 > 23.8 \text{ mag/arcsec}^2$, $[\alpha - \alpha(\text{true})]/\alpha = -0.1 \pm 0.12$.

5.1. Classification Efficiency

To measure the number density of LSBs, we must determine the efficiency with which we can both detect and identify LSBs as a function of surface brightness and size. As discussed above (§4), because our classification procedure effectively eliminates LSBs with bulges from the final sample, we need only to test the recovery of pure disk exponential profile galaxies in order to measure our efficiency. While doing so means that we will not be measuring the efficiency of detecting all LSBs (i.e. LSBs with and without bulges

and/or bright HII regions, which are seen to exist in brighter LSB samples), we know *a priori* that our classification procedure reduces the efficiency of finding such galaxies in our final sample to zero, given that the surface brightness profiles and images demonstrate that none of these galaxies with more complicated morphologies have made it into the final sample. Thus, the population of LSB disks with associated bulges and bright HII regions is entirely unconstrained by this paper, and the measured number density will be an underestimate of the true LSB population. Furthermore, because the galaxies in our sample are all smooth exponential disks with low ellipticities (with the possible exception of Q-42-1), measuring the efficiency of the survey requires only that we test the recovery of similarly smooth, face-on, exponential disks.

To first measure our ability to classify LSBs, we added 100 artificial LSBs to various positions throughout the original imaging data and then clipped out the region containing the LSB, creating an image identical in size to the images which were used for classification in the actual survey. The pure exponential face-on disks used as test LSBs were morphologically indistinguishable from the LSBs in the sample, which also have pure exponential profiles and low ellipticity. As a result, the images of the artificial LSBs appeared remarkably similar to the true LSB images (see Figure 2). We inspected and classified the artificial LSBs, in the same manner as the actual survey data. Figure 1(a) shows the resulting classifications as a function of exponential scale length and surface brightness; the triangles were classified as LSBs and the diagonal lines are lines of constant signal to noise (i.e. $\mu_0 = \mu_{zp} + 2.5 \log \alpha$, with varying μ_{zp} , and α measured in arcseconds). Figure 1(b) shows the resulting classification efficiency as a function of signal-to-noise (characterized by μ_{zp}), for $\alpha > 2.5''$ (for scale lengths smaller than $2.5''$, the classification ability drops dramatically, due to confusion between single, low redshift LSBs and pairs of faint, distant normal galaxies). Our classification efficiency is essentially 100% for $\mu_{zp} < 22.2 \text{ mag/arcsec}^2$, and zero for $\mu_{zp} > 22.95 \text{ mag/arcsec}^2$. We approximate the efficiency in Figure 1(b) analytically as

$$\epsilon_{class} = \begin{cases} 1 & \text{if } \mu_{zp} \leq 22.2 \\ \frac{22.95 - \mu_{zp}}{22.95 - 22.2} & \text{if } 22.2 < \mu_{zp} < 22.95 \\ 0 & \text{if } 22.95 \leq \mu_{zp}, \end{cases} \quad (1)$$

which has a residual rms of 0.094 for $21.8 < \mu_{zp} \leq 22.95$.

Based upon equation 1, we make the final restriction on the subset of LSBs, retaining only those galaxies for which $\alpha > 2.5''$ and $\mu_{zp} \equiv \mu_0 - 2.5 \log \alpha \leq 22.95$. This leaves a final LSB catalog of 7 galaxies which have securely measured classification efficiencies. The classification images of these LSBs are shown in Figure 2 (including also the cleaned and smoothed images, as described in §4). Their radial profiles are shown in Figure 3, and their structural properties are listed in Table 1.

5.2. Detection Efficiency

In addition to our efficiency in classifying LSBs, we must also quantify our ability to detect LSB candidates in the first place. To do so, we used monte carlo simulations to measure the efficiency with which our automatic detection software identified the smoothed fluctuations produced by artificial galaxies, as a function of central surface brightness and exponential scale length.

First, a single artificial, face-on galaxy with an exponential profile was added to an image from the survey. The artificial galaxies were drawn from a uniform distribution in $\log \alpha$ and central surface brightness, between $1'' < \alpha < 125''$ and $23 < \mu_0 < 28.25 \text{ mag/arcsec}^2$, above a fixed signal-to-noise ($\mu_0 < 2.5 \log \alpha + 26.5 \text{ mag/arcsec}^2$). The altered image was processed in an identical manner to the original

survey data. The resulting catalog of low surface brightness objects was searched for any detection that coincided with the artificial galaxy. This process was repeated five times for each image in the survey.

The small surface density of true objects (≈ 1.0 per frame) implies that confusion and overlapping of low surface brightness objects is not a source of selection biases in the survey. Thus, the Monte Carlo simulations were designed to test the recovery of isolated galaxies, by requiring that there was at least a $40''$ buffer between an artificial galaxy and the nearest candidate LSB. However, the detection efficiencies are modulated by any residual large scale variations in the background sky level, with more objects being detected in areas where the local sky is higher than average. Therefore, if too large a buffer is required between the artificial galaxies and the real objects, then the artificial galaxies will be systematically biased away from these regions of increased detection efficiency. The largest fluctuations occur on scales of $\approx 2'$, so by limiting the buffer to $40''$ (substantially smaller than the width of the strip) we have allowed the artificial galaxies to sample the same sky levels as the real detections.

Figure 4(a) shows the resulting detection efficiency for our survey, as a function of surface brightness and disk scale length. Superimposed on the contours of constant efficiency are all the LSBs with $\mu_0 > 23 \text{ mag/arcsec}^2$, as well as the regions of 100% and $> 0\%$ classification efficiency. Within the region where LSBs can be reliably classified, the detection efficiency is well behaved, as can be seen in Figure 4(b), where we have plotted the detection efficiency as a function of scale length, for different central surface brightnesses. The distribution is reasonably well fit by a Gaussian, leading us to use

$$\epsilon_{det} = 0.37 \exp \left[-\log^2 (\alpha/6.3'')/0.15 \right] \quad (2)$$

as a reasonable approximation of the detection efficiency for the final LSB subsample. The residual rms of this approximation is 0.056. The maximum detection efficiency is roughly 35%, which results largely from the loss in area behind masks, behind other stars and galaxies, and around the edges of the images. The detection efficiency peaks close to the scale length of the $5''$ exponential smoothing filter used in processing. The contours of constant detection efficiency suggest that LSBs with $\mu_0 = 26 \text{ V mag/arcsec}^2$ may be in the full catalog, but be currently unclassified or misclassified as clusters.

We have not attempted to model edge-on LSBs. Including edge-on LSBs could have easily introduced more uncertainty than it would have removed; we know very little about the vertical scale heights and opacities of LSB disks, particularly at the extreme surface brightnesses explored by this survey. Furthermore, none of our detected LSBs is substantially elongated, and thus the detection efficiency for edge-on LSBs is not an essential ingredient for recovering the LSB number density of the smooth face-on LSBs in our sample. However, since we are strongly biased against finding edge-on LSBs, due to our choice of a circularly symmetric smoothing filter, we may well be underestimating the number density of LSBs by effectively restricting our sample to include mostly face-on galaxies.

5.3. Distances

Follow-up spectroscopy of the final LSB subsample was carried out in May of 1996 using the CryoCam on the Mayall 4m at Kitt Peak National Observatories. The 650 grism (400 line/mm) was used in first order with a $3.2''$ slit, giving $\sim 13\text{\AA}$ resolution (FWHM) between 3500\AA and 7000\AA , with an average of 3\AA per pixel. The slit was oriented along the major axis of the LSB, using the Richley prisms to correct for the differential refraction of the atmosphere. Exposure times ranged from 2700s to 12,000s giving a

signal-to-noise of 10-40 per resolution element longwards of the the 4000Å break, with a mean signal-to-noise of 15-20.

The spectra of the LSBs were overscan corrected, dark subtracted, flat-fielded using domeflats, illumination corrected with twilight flats, and then extracted, sky subtracted, and wavelength calibrated using He+Ne+Ar spectra taken adjacent to, or sandwiched between, each of the LSB spectra. The focus of the spectrograph was a strong function of wavelength, and degrades by nearly a factor of two by 3600Å.

The resulting LSB spectra were initially cross-correlated with a template spiral galaxy spectrum using IRAF’s “rvsao” package, and searched for emission lines. The cross-correlation was limited to between 3700Å and 5000Å to isolate the 4000Å break, the Balmer lines, and the strong G-band. Since all galaxies were at very low redshift, the correlation included nearly the same region of the rest-frame spectra for all galaxies. Using the resulting redshifts, the spectra were doppler corrected back to zero redshift. Then, to refine the redshift measurement, we created an improved correlation template for each galaxy, by coadding all the other LSB spectra, excluding the one galaxy spectra to be cross-correlated and the spectra for R-26-1, which has low signal-to-noise and thus no convincing redshift. The new templates were then cross-correlated with the correct galaxy spectra and a new redshift derived. The process was repeated a second time using templates derived from the refined redshifts. On the final cross-correlation, no redshift changed by more than 450 km/s, and all correlation coefficients had $4.4 < R < 7.6$, with the exception of M-232-1, which had $R = 3.7$, and R-26-1, for which we have no convincing redshift. The emission line redshifts for R-27-1 and Q-129-2 were within 400 km/s of the cross correlation absorption line redshifts. We take this velocity difference to be representative of the 1σ uncertainty in the individual redshifts, although the formal error from the cross-correlation is smaller ($\lesssim 200$ km/s). Similar changes in the velocity were produced by changing the wavelength range and filter parameters used for the cross-correlation, again suggesting that the redshifts given in Table 1 are accurate only to several 100 km/s. In all cases, however, the cross-correlation functions do not have additional peaks which could be considered as alternative plausible redshifts. The redshift for M-232-1 is more uncertain, due to the lower signal-to-noise and as can be seen from the lower correlation coefficient. By eye, we find a limit of ± 1000 km/s on the error in the redshift. The final redshifts are listed in Table 1, and the spectra are shown in Figure 5, along with the template spectra used for cross-correlation, all shifted into the rest frame; because of the low redshifts, the shift was only ~ 100 Å. For the purposes of analysis, we assign a redshift to R-26-1 by assuming it has the mean physical scale length of galaxies in the sample ($h = 2.9$ kpc), giving an assumed recessional velocity of 11600 km/s. If R-26-1 were to have the smallest or largest physical scale length of the sample, it would have recessional velocities of 6800 km/s or 14600 km/s respectively.

The LSBs have recessional velocities of 4000-9000 km/s, and disk scale lengths of $1.7 - 3.6 h_{50}^{-1}$ kpc (Table 1, excluding R-26-1, due to its uncertain redshift), comparable to the disk scale lengths seen in angular diameter limited field surveys of brighter LSBs (McGaugh & Bothun 1994, de Blok et al 1995, de Jong 1996) and of normal galaxies. The LSBs in the final subsample are also at comparable distances to normal galaxies catalogued in large local surveys. The similarity can be seen most readily in Figure 6, where we have plotted a “pie” redshift-position diagram for the final LSB sample (solid triangles) and for the galaxies in the ZCAT catalog of galaxies (open circles). The LSBs also have scale lengths which are similar to normal galaxies. Both the LSB and normal galaxy samples will be biased towards finding physically large galaxies, which have the largest probability of being identified in angular diameter limited surveys (see Appendix B).

Figure 6 shows that there is no strong tendency for the LSBs in our sample to be physically associated with normal galaxies. Between 3000 km/s and 10000 km/s, 11 out of 23 ZCAT galaxies are in close

associations, whereas 2 in 6 of the LSBs has a near neighbor. Because of the small numbers of LSBs and the non-uniform selection criteria for the ZCAT galaxies, our sample does not provide definitive evidence for the low correlation between LSBs and normal galaxies. However, it is suggestive of the general trend seen in brighter LSB samples for the small-scale correlation of LSBs to be weak compared to normal galaxies (Bothun et al. 1993, Mo et al. 1995).

The follow-up, spectroscopic observations also provide validation for our classification procedure. All of the candidate LSBs in the final sample which we observed spectroscopically have characteristic galaxy spectra, smooth light profiles perpendicular to the dispersion direction, and low redshifts, proving that the final sample includes only the nearby LSBs which the survey was designed to find. While our classification procedure may have missed LSBs (i.e. false negatives), our strict selection criteria (§5.2 & 5.1) successfully insured that we did not include any non-LSBs in our final candidate list (i.e. false positives).

6. The Number Density of LSBs

Using the classification and detection efficiencies from equations 1 & 2 we can correct for the area that was effectively lost from the survey and calculate the surface density of LSBs with $23 < \mu_0 < 25$ V mag/arcsec 2 . The total efficiency $\epsilon(\mu_0, \alpha) = \epsilon_{class}(\mu_0, \alpha) \times \epsilon_{det}(\mu_0, \alpha)$ is a measure of the fraction of the total 17.48 degree 2 survey area which was actually accessible for detecting an LSB with central surface brightness μ_0 and exponential disk scale length α . Using the formalism developed in Appendix A, the surface density of LSBs in our survey with $23 < \mu_0 < 25$ mag/arcsec 2 and $\alpha > 2.5''$ is:

$$\Sigma(23 < \mu_0 < 25 \text{ mag/arcsec}^2, \alpha > 2.5'') = 4.1_{-2.1}^{+2.6} \text{ galaxies/degree}^2, \quad (3)$$

where the errors enclose 90% confidence. The uncertainty is dominated by the Poisson probability for 7 galaxies and a detailed calculation of the confidence interval is provided in Appendix A. While a naive calculation of the surface density (7 galaxies in 17.5 square degrees) gives a smaller surface density, inspection of Figure 4(A) for $\alpha > 2.5''$ shows that the detection and classification efficiencies are small over much of the region, leading to a large correction. As shown in Appendix B, the surface density of galaxies on the sky increases as α^{-4} towards small angular sizes, and thus most of the correction applied to the measured surface density is a correction for the lost classification efficiency of small galaxies with $\mu_0 > 24$ mag/arcsec 2 . Furthermore, because of the steep increase in the number of galaxies with small apparent scale lengths, the surface density is a strong function of the exact lower limit on α , and thus LSB surveys with different angular selection criteria will derive very different surface densities.

Although the surface density may at first seem small, it is in fact significant, given that the large scale lengths to which the sample was restricted effectively confines the survey to a small, nearby volume. The low surface density also explains why there is a consistent impression that LSBs are rare. First, one would have to observe a square degree of the sky to be reasonably certain of finding one large LSB. Second, the LSB would appear much smaller than a normal galaxy of comparable scale length, because it would only be visible out to roughly one scale length before its surface brightness drops below the pixel-to-pixel variations in the sky; normal galaxies are visible out to several scale lengths and thus are more noticeable (Disney & Phillips 1983).

Using the distances for the final LSB subsample, the efficiency for detection and classification and the selection criteria for the final sample, we can calculate the effective volume in which each LSB could be

detected. An LSB at a distance D_i , with angular scale length α_i and central surface brightness μ_i could have been detected out to a distance of

$$D_{max_i} = D_i \times \begin{cases} \frac{\alpha_i}{2.5''} & \text{if } \mu_i < 22.95 + 2.5 \log 2.5'' \\ \frac{\alpha_i}{10^{0.4(\mu_i - 22.95)}} & \text{if } \mu_i \geq 22.95 + 2.5 \log 2.5'' \end{cases}. \quad (4)$$

The effective volume of the survey is different for each galaxy, because the detection efficiencies are a strong function of the angular scale length and central surface brightness of the individual galaxies.

Using D_{max} , the volume that the i th galaxy could be detected within is

$$V_i = \frac{A}{\text{radians}} \int_0^{D_{max_i}} \epsilon(\mu_i, \alpha_i) \left[\frac{D_i}{D'} \right] D'^2 dD' \quad (5)$$

$$= \frac{A}{\text{radians}} [\alpha_i D_i]^3 \int_{\frac{\alpha_i D_i}{D_{max_i}}}^{\infty} \frac{\epsilon(\mu_i, \alpha')}{\alpha'^4} d\alpha', \quad (6)$$

including the change in detection efficiency with the apparent angular size; because the efficiency changes with distance, the survey volume associated with a given galaxy is not a simple conical section, but tapers off as D approaches D_{max} . There is no minimum distance at which an LSB can be detected, because we imposed no upper limit on the angular size of galaxies within our survey. There is an implicit upper limit set by the width of the survey fields, but the limit is so much larger than the angular scales of the galaxies in the survey that the effective minimum distance is zero.

With equations 4 and 5, the total number density of LSBs with $23 < \mu_0 < 25 \text{ mag/arcsec}^2$ and intrinsic scale lengths h between $1.7 h_{50}^{-1} \text{ kpc}$ and $3.6 h_{50}^{-1} \text{ kpc}$ is

$$\mathcal{N}(23 < \mu_0 < 25 \text{ mag/arcsec}^2, 1.7 < h < 3.6 h_{50}^{-1} \text{ kpc}) = \sum_{i=1}^n \frac{1}{V_i} = 0.01^{+0.006}_{-0.005} \text{ galaxies/h}_{50}^3 \text{ Mpc}^3, \quad (7)$$

with 90% confidence, assuming the probability distributions derived in Appendix A. As with the measurement of the surface density, the uncertainty is entirely dominated by the uncertainty due to the small number of galaxies in the final LSB subsample. The value of \mathcal{N} changes negligibly other reasonable redshifts for R-26-1 are used.

In order to compare the relative contribution of LSBs and normal galaxies, Figure 7 shows the integrated number density of LSBs with central surface brightness fainter than 23 mag/arcsec^2 in V , as a function of limiting surface brightness. Superimposed on the integrated LSB number density are comparable measurements of the integrated number densities of normal galaxies, for several different determinations of the local luminosity function. To make “comparable” integrated number densities of normal galaxies we have restricted the integration to either (1) the range of absolute magnitude covered by the LSBs in our sample ($-16.1 > M_V + 5 \log h_{50} > -18.6$) or (2) the range of intrinsic exponential disk scale lengths of our sample ($1.7 - 3.6 h_{50}^{-1} \text{ kpc}$) (assuming that a normal galaxy’s scale length can be determined from its luminosity, if it has a Freeman central surface brightness of $21.7 \text{ mag/arcsec}^2$ in B and $\langle B - V \rangle \sim 0.5$). The corresponding number densities are labelled in Figure 7 as “same M ” and “same α ”, respectively.

As Figure 7 shows, the integrated number density of LSBs with central surface brightness fainter than 23 mag/arcsec^2 in V is *greater* than the number density of normal galaxies with either similar luminosities or similar scale lengths. We consider this result to be extremely robust. The errors are dominated by the well-understood Poisson statistics of the small number of LSBs, and thus, only an egregious, systematic error in the measured distances or in the integrated efficiencies (eqn 5) could produce a large enough effect to change our conclusions. In spite of the small numbers of LSBs in the final sample, the large number density of LSBs would persist even if significant fractions of the sample were to be removed. For example, even between 23 mag/arcsec^2 and 24 mag/arcsec^2 , the number density of LSBs remains comparable or greater than normal galaxies. Our conclusions hold as well if the confidence intervals are increased to 99%.

We have also considered the degree to which photometric errors could effect our measurement of \mathcal{N} , by examining $1/V_i$ as a function of central surface brightness μ_0 . Brighter than $\mu_0 = 24 \text{ mag/arcsec}^2$, the effect of photometric errors is very small, such that an error of 1 magnitude in the zero point changes the derived number density by less than a factor of two, due to variations in the integral over the efficiency. The effect is stronger for fainter central surface brightnesses, where the overall efficiency is lower and more sensitive to μ_0 . Even so, the required zero point error would need to be larger than the observations admit. For example, to reduce the number density for $\mu_0 > 24 \text{ mag/arcsec}^2$ by a factor of 10 (which would still leave \mathcal{N} comparable to the normal galaxy number density), the zero point would have to be systematically 0.9 magnitudes too faint in the fields containing the faintest LSBs. From our photometric calibration, we believe that our mean zero point is good to at least 0.1 magnitudes, so there would have to be a temporary fluctuation in the zero point of the strip scan while the LSBs were passing overhead. Such a shift would have produced nearly a factor of 3 drop in the mean number of objects per field, based upon the number counts of Postman et al. (1996) and would probably have been accompanied by a brightening of the sky level. Neither of these signatures is seen, given that the data was originally restricted to the parts of the strip scan which were stable in both sky brightness and number of detected objects. The number of objects never varies by more than 25% in either the RMS or the mean, suggesting that the zero point does not fluctuate by more than 0.25 magnitudes, based upon the number counts. This is a strong upper limit, given that simple Poisson statistics contributes 10% to the RMS component and that the lost detection area due to bright stars probably makes a similar contribution. The maximum zero point uncertainty suggests that, for $\mu_0 > 24 \text{ mag/arcsec}^2$, the most we could have possibly overestimated an individual galaxy's contribution to the number density is a factor of 2, which is still contained within the 90% confidence interval. Thus, the total measurement of \mathcal{N} could be high by at most a factor of 2, and only in the unlikely event that every LSB in the sample had the largest possible zero point error, in exactly the same direction.

We have reasons to believe that, if anything, our measurement of \mathcal{N} is an underestimate. First, our choice of a circularly symmetric smoothing filter greatly reduces our sensitivity to edge-on LSBs, and thus we are only sensitive to the fraction of galaxies which are seen relatively close to face-on. This limitation is evident in the fairly circular morphologies of all of the galaxies found in the survey. Second, we have been extremely conservative in our decision to classify detections as possible LSBs. We have consciously excluded possible LSBs which we feel cannot be adequately distinguished from clusters or tidal extensions off bright galaxies. Thus LSBs with small HII regions or central bulges are not included in our sample, and we are restricted to finding only LSBs which have classical Im morphologies. There is a tendency for higher luminosity, large scale length LSBs to be earlier Hubble types (McGaugh, private communication), and thus we are less sensitive to the most luminous LSBs. This bias will lead us to underestimate the luminosity density even more severely than we are underestimating the number density. Note also that the galaxies which we have identified have very regular, smooth morphologies, allowing us to accurately simulate their detection and classification efficiencies.

In Figure 7, the overdensity of LSBs is smaller when compared to the AutoFib survey luminosity function (Ellis et al. 1996), than when compared to the Stromlo-APM (Loveday et al. 1992) or DARS (Peterson et al. 1986) surveys, which both have limiting magnitudes of $b_j \approx 17$. However, the AutoFib survey combines the shallower DARS survey with much deeper pencil beam surveys which reach limiting isophotal magnitudes of $b_j \approx 24$. As discussed by McGaugh (1994), this implies that the AutoFib survey has a fainter surface brightness limit than the shallower Stromlo-APM or DARS surveys. Thus, the AutoFib survey is likely to have cataloged far more intrinsically low surface brightness galaxies than the shallow nearby surveys, increasing the integrated number density implied by the AutoFib luminosity function over what is measured in shallower surveys; this is clear from the integrated number densities plotted in Figure 7. (Note also that the AutoFib luminosity function has the steepest faint-end slope of the three surveys.) The different surface brightness ranges of the surveys, therefore, changes the apparent relative importance of the LSB and normal galaxy population.

The integrated luminosity density of LSB galaxies is presented in Figure 8, along with the integrated luminosity density in normal galaxies. When restricted to the same range in absolute magnitude, normal galaxies and LSB with $\mu_0 > 23 \text{ mag/arcsec}^2$ and $1.7 - 3.6 h_{50}^{-1} \text{ kpc}$ make a comparable contribution to the total luminosity density of the universe. However, when restricted to the same range in scale length, the higher luminosity, high surface brightness disks dominate the luminosity density by factors of 2-6 over the LSB component, as might be expected by the drastic difference in intrinsic luminosity. There is also very little evidence for a major contribution to the luminosity density from galaxies whose disks are fainter than $\mu_0 = 24 \text{ mag/arcsec}^2$ in V ; even if there is possible evidence for a rise in number density with decreasing surface brightness in Figure 7, it is not enough to compensate for the increasing faintness of the disk. We should note however, that these results apply only for a limited range of galaxy properties, and should not be applied more generally. Because of our bias against LSBs with bulges, we may be systematically excluding the most luminous galaxies from our sample, and thus our conclusions only hold for the range of disk scale lengths and absolute magnitudes covered by our sample. Our calculated contribution of LSBs with $\mu_0 > 23 \text{ mag/arcsec}^2$ to the luminosity density is comparable to that calculated in the brighter APM LSB survey (Sprayberry et al. 1997).

We may compare the measured relative number densities and luminosity densities for LSBs and normal galaxies to those which are predicted by the formalism presented in Dalcanton et al. (1997). We do so by integrating the predicted galaxy number density for central surface brightnesses between $23.5 \text{ mag/arcsec}^2$ and $25.5 \text{ mag/arcsec}^2$ in B (assuming $\langle B - V \rangle \sim 0.5$ for the LSBs in our sample), and intrinsic disk scale lengths between $1.7 - 3.6 h_{50}^{-1} \text{ kpc}$, and comparing it to the integrated predicted number density for comparable normal galaxies, with “comparable” defined as in Figure 7, and assuming $20 < \mu_0 < 22.5 \text{ mag/arcsec}^2$ for the galaxies which are typically used to determine the local luminosity function; this limit is most appropriate for the DARS and Stromlo-APM surveys. We make a similar calculation of the luminosity density. For the theoretical models, we have assumed the values of the values of $\Upsilon = 3 M_\odot / L_\odot$ for the mass-to-light ratio of baryons, $F = 0.05$ for the baryonic mass fraction, and $M_* = 10^{12} M_\odot$, and $\alpha_{lum} = -1.5$ for the Schechter function describing the distribution of galaxy masses.

We find that the predicted ratio of the number density in LSBs to the number density in normal galaxies with similar scale lengths is 2; this ratio varies somewhat with variations in the limiting surface brightness for normal galaxy surveys between $22.0 \text{ mag/arcsec}^2$ and 23 mag/arcsec^2 . The predicted ratio is therefore in agreement with what is measured in Figure 7. Restricting the normal galaxy sample to have similar absolute magnitudes to the LSB sample, the predicted ratio becomes 0.3. The agreement between the measured and predicted relative number density is not as good in this case, with there being even

more LSBs measured than predicted. However, comparing the same range of absolute magnitude is much more sensitive to the faint-end slope of the luminosity function at very faint magnitudes. Because of the rapid rise in number density with decreasing luminosity, the integrated number density depends strongly on the number density of the faintest galaxies ($M_V + 5 \log h_{50} \sim -16$ in this case); unfortunately, this limiting absolute magnitude is where the local luminosity function is most poorly determined, and may be extremely incomplete (Driver & Phillipps 1996). The discrepancy may also result from the parameters of the theoretical model. We have assumed that the theoretical mass function of galaxies has a steep faint-end slope of -1.5 , which greatly inflates the number of low-mass galaxies relative to high-mass galaxies; this accounts for the large difference seen in the predicted ratio of number densities when the normal galaxies are restricted to similar absolute magnitudes rather than similar scale lengths. We have also assumed that a galaxy's mass is uncorrelated with its angular momentum, whereas in the BBKS formalism (Bardeen et al. 1996), there should be a correlation wherein low mass galaxies tend have higher angular momenta (Catelan & Theuns 1996). This correlation would increase the expected ratio of LSBs to normal galaxies in a fixed magnitude range.

We see a similar level of agreement between the predicted and measured relative luminosity densities. The predicted ratio of luminosity densities of normal galaxies to LSBs with the same range of scale lengths is ~ 6 , which also agrees reasonably well with the observations (Figure 8. When restricted to the same range of absolute magnitude the predicted ratio of normal galaxy luminosity density to LSB luminosity density is 4, whereas they are observed to be comparable. This suggests that there is more luminosity density in LSBs than predicted. Again, uncertainty in the measured faint-end of the local luminosity function, or a correlation between mass and angular momentum could bring these into agreement.

7. Conclusions

The importance of the low surface brightness galaxy population has been an outstanding question in astronomy. Claims have ranged from LSBs being a negligible component of the local universe (Roukema & Peterson 1994) to outnumbering $L > 0.1L_*$ galaxies by orders of magnitude ($\mathcal{N} = 1 \text{ Mpc}^{-3}$ for scale lengths greater than 0.8 kpc; Schwartzenberg et al. 1995). To address this recent debate, we have presented the first well-quantified measurement of the absolute number density and luminosity density of low surface brightness galaxies, using a large area CCD survey with well understood selection criteria, quantifiable detection efficiencies and follow-up spectroscopy of all LSB candidates. Our survey has selected LSBs which are comparable to the galaxies in the NGC catalog, in both size and distance, allowing a direct, meaningful comparison with local field galaxy surveys.

We find that the number density of LSB galaxies with $23 < \mu_0 < 25 \text{ V mag/arcsec}^2$ is indeed greater than the number density of normal galaxies, when the normal galaxies are restricted to the same range in either absolute magnitude ($-16.1 > M_V + 5 \log h_{50} > -18.6$) or in exponential disk scale length ($1.7 - 3.6 h_{50}^{-1} \text{ kpc}$). The exact ratio depends upon which local luminosity function is used for comparison, but LSBs typically outnumber comparable normal galaxies by factors of 2 or more. The measured ratios are formally consistent with theoretical expectations based on assuming that high angular momentum and/or low mass protogalaxies collapse to form low surface brightness galaxies (Dalcanton et al. 1997).

However, we also find that LSBs with central surface brightnesses fainter than $23 \text{ V mag/arcsec}^2$ and with scale lengths between $1.4 - 3.6 h_{50}^{-1} \text{ kpc}$ make a less significant contribution to the luminosity density of the universe. In our survey, galaxies fainter than $24 \text{ V mag/arcsec}^2$ make almost no contribution to the

luminosity density, and galaxies fainter than $23 V \text{ mag/arcsec}^2$ contribute 15-50% of the luminosity density contributed by comparable normal galaxies. Thus, a significant (but not overwhelming) fraction of the stars, and perhaps the mass, of the universe is in LSBs.

The inferred number densities and luminosities are likely lower limits as the survey may have excluded significant number of LSBs due to selection effects. By design, our survey does not include galaxies which are intermediate in surface brightness between $23 V \text{ mag/arcsec}^2$ and the characteristic Freeman surface brightness; these galaxies are intrinsically more luminous, and thus could make a much larger contribution to the luminosity density. Furthermore, we have restricted our selection to Sm/Im morphologies, whereas the brightest, largest scale length LSBs tend to have both bulges and spiral arms (McGaugh; private communication). This bias against earlier type morphologies may well have lead us to underestimate the LSB luminosity density, and, less severely, the LSB number density. Our survey also includes a strong bias against edge-on LSBs (due to using a circularly symmetric filter in the detection algorithm), which may again lead us to underestimate the LSB density.

Acknowledgements

Tony Tyson and Ian Smail are warmly thanked for advice on the photometric calibration, as is Lori Lubin for her assistance with data acquisition at the KPNO 0.9m and Jim DeVeny for his help with the CryoCam at the KPNO 4m. Tony also generously donated huge quantities of disk space, without which this project could not possibly have been done. The referee is also thanked for very helpful commentary and suggestions. JJD gratefully acknowledges useful discussions with Rebecca Bernstein and Dan Rosenthal. Support for JJD was provided by NASA through Hubble Fellowship grant #2-6649 awarded by the Space Telescope Science Institute, which is operated by the Association of Universities for Research in Astronomy, Inc., for NASA under contract NAS 5-26555. Partial support for DPS provided by National Science Foundation grant AST-95-09919. MS was supported by NSF grants AST91-08834 and AST94-15574.

Appendix A

Probability Distributions for Σ and \mathcal{N} for Small Numbers of Galaxies

Suppose we have a sample of n galaxies, the i th which has angular scale length α_i and central surface brightness μ_i . Assume that there is a unique overall detection efficiency $\epsilon(\alpha, \mu)$ associated with each scale length and surface brightness, and that there is a fixed rms uncertainty in ϵ of σ_ϵ .

Assuming that the underlying galaxy distribution in surface brightness and apparent scale length is $f(\mu)f(\alpha)$, the total number \bar{N} of galaxies expected in a survey of area A with central surface brightnesses between μ_1 and μ_2 and apparent angular scale lengths greater than α_1 is:

$$\bar{N} = \int_{\mu_1}^{\mu_2} \int_{\alpha_1}^{\infty} f(\mu)f(\alpha) \epsilon(\alpha, \mu) d\mu d\alpha. \quad (1)$$

If the survey had perfect efficiency, $\epsilon \equiv 1$, the survey would recover

$$\bar{N}_0 = \int_{\mu_1}^{\mu_2} \int_{\alpha_1}^{\infty} f(\mu)f(\alpha) d\mu d\alpha \quad (2)$$

galaxies. Thus, the total survey efficiency is \bar{N}/\bar{N}_0 . Suppose then, that an individual survey measures n galaxies over the survey area. The surface density becomes

$$\Sigma = n \frac{\bar{N}}{\bar{N}_0} \frac{1}{A}. \quad (3)$$

As shown in Appendix B, for local volumes where cosmological curvature is negligible, $f(\alpha) = \alpha^{-4}$ for any distribution of intrinsic galaxy scale lengths. We have assumed that μ and α are independent variables, and have the freedom to choose any distribution of $f(\mu)$. We take $f(\mu)$ to be constant to first order, as is consistent with the data presented in Figure 7.

To calculate the probability distribution of the surface density Σ , we first consider the effect of having a small number of galaxies in the sample. We calculate this Poisson uncertainty by adopting Bayes Theorem. We assume that, given a single trial which measured n events, the probability that infinite number of similar trials would measure a mean of \bar{n} events is $p_n(\bar{n}|n) \propto p(n|\bar{n})p(\bar{n})$. Because we have no prior reason to prefer any value of \bar{n} , we assume that the prior probability $p(\bar{n})$ is uniform, and thus that $p_n(\bar{n}|n) \propto p(n|\bar{n})$, which is simply the Poisson probability of observing n events for a system which would give a mean of \bar{n} events.

There is also a contribution to the uncertainty in Σ from the uncertainty in the efficiency ϵ . However, the integral in equation 3 averages out much of the uncertainty in the efficiency ϵ . For the particular example of our survey, while the pointwise estimation of ϵ_{class} and ϵ_{detect} has an rms uncertainty of roughly 0.1, the integral over the efficiency in equation 1 is much more tightly constrained. The uncertainty contributed to the integral by ϵ_{class} is negligible ($\sim 1\%$), and the uncertainty contributed by ϵ_{detect} is likewise small ($< 10\%$) for central surface brightnesses fainter than 23.5 mag/arcsec². At brighter surface brightnesses, our approximation for ϵ_{detect} overestimates the integral volume by $\sim 50\%$. However, we only have one galaxy in this surface brightness interval, and the direction of the error is to underestimate the number density, thus we expect this to contribute very little uncertainty to the total number density. Given that the Poisson uncertainty is of the order of 40% for our sample, we will neglect the contribution of $p_{\epsilon_i}(\epsilon)$ to the uncertainty in Σ . Thus, the final probability distribution for the surface density Σ is

$$p(\Sigma) = p_n(\bar{n}|n = A\Sigma \frac{\bar{N}_0}{\bar{N}}) A \frac{\bar{N}_0}{\bar{N}}. \quad (4)$$

We may also solve for the effective number density of the survey, given the distance D_i of each galaxy, and the maximum distance at which each galaxy could be detected, D_{max_i} (eqn. 4). The effective volume associated with each galaxy, V_i , is an integral over distance, accounting for the changing efficiency with changing angular size:

$$V_i = \frac{A}{\text{radians}} \int_0^{D_{max_i}} \epsilon(\mu_i, \alpha_i) \left[\frac{D_i}{D'} \right] D'^2 dD' \quad (5)$$

$$= \frac{A}{\text{radians}} [\alpha_i D_i]^3 \int_{\frac{\alpha_i D_i}{D_{max_i}}}^{\infty} \frac{\epsilon(\mu_i, \alpha')}{\alpha'^4} d\alpha', \quad (6)$$

assuming that the galaxies are close enough that $(1+z)^4$ cosmological dimming of μ can be neglected. With the exception of the integral over surface brightness, this integral is identical to the one equation 1.

The uncertainties in each volume term V_i are dominated by the Poisson uncertainties which also dominate the calculation of Σ (here, $n = 1$). The other possible contributions are from the uncertainty in the measurement of α_i , which is $\sim 10\%$, and in D_i , which is less than 5%. These are also negligible

compared to the Poisson uncertainties; in the limit of Gaussian statistics, including a 10% uncertainty from the detection efficiency and a 10% efficiency from the measurement of α_i would increase a 40% Poisson uncertainty to only 42%.

The number density, \mathcal{N} , measured for the sample of n galaxies is

$$\mathcal{N} = \sum_{i=1}^n \frac{1}{V_i}. \quad (7)$$

With our assumption that Poisson statistics dominate uncertainties in V_i , the probability for the individual terms $\mathcal{N}_i = 1/V_i$ is $p_{\mathcal{N}_i} = p_n(\mathcal{N}_i V_i | 1) V_i$. The final probability distribution of \mathcal{N} is then

$$p_{\mathcal{N}}(\mathcal{N}) = A \int_0^\infty p_{\mathcal{N}_1}(\mathcal{N}'_1) \int_0^\infty p_{\mathcal{N}_2}(\mathcal{N}'_2) \int_0^\infty \cdots \int_0^\infty p_{\mathcal{N}_{n-1}}(\mathcal{N}'_{n-1}) p_{\mathcal{N}_n}(\mathcal{N} - \sum_{i=1}^{n-1} \mathcal{N}_i) d\mathcal{N}'_1 d\mathcal{N}'_2 \cdots d\mathcal{N}'_{n-1}, \quad (8)$$

which can be solved with Monte Carlo integration by repeatedly drawing samples of galaxies from each of the $p_{\mathcal{N}_i}(\mathcal{N}_i)$.

Appendix B

Recovering the Number Density and Scale Length Distribution of LSBs from the Observed Surface Density

In this Appendix we investigate the relationship between the intrinsic number density of objects at redshift z with surface brightness μ_0 and physical scale length R , $N(\mu_0, R, z)$, and the observed surface density of objects with apparent surface brightness μ and angular scale length α , $\Sigma(\mu, \alpha)$. We also calculate the underlying distribution of LSB scale lengths from existing catalogs.

First, consider a volume element $dV(z)$ at an angular diameter distance $D_a(z)$, subtending one steradian of the sky. The number density of objects in the shell that appear with angular scale length α is

$$N(\mu_0, \alpha, z) = N(\mu_0, R = \alpha D_a(z), z) \frac{R}{\alpha}, \quad (1)$$

where α is measured in radians. If we allow objects to be at large enough distances that surface brightness diminution plays a role, then the observed surface brightness scales as $(1+z)^{-4}$ and the number density becomes

$$N(\mu, \alpha, z) = N(\mu_0 = \mu - 10 \log(1+z), \alpha, z) \quad (2)$$

The number of objects per steradian per mag/arcsec² is

$$\Sigma(\mu, \alpha) = \int_0^\infty N(\mu, \alpha, z) dV(z). \quad (3)$$

If a sample is close enough that all distances can be treated as Euclidean, the volume element is $D_a^2 dD_a = \alpha^{-3} R^2 dR$, the surface brightness of a galaxy does not change with distance, and evolution in $N(\mu_0, \alpha, z)$ may be safely ignored. Therefore, for a uniform distribution of galaxies, Equation 3 becomes

$$\Sigma(\mu, \alpha) = \frac{1}{\alpha^4} \int_0^\infty N(\mu_0 = \mu, R) R^3 dR. \quad (4)$$

Note that $\Sigma(\mu, \alpha)$ will always be proportional to α^{-4} , independent of the distribution of intrinsic scale lengths. Any size galaxy can be seen to a larger distance if it is observed at a smaller limiting angular size; smaller values of α always probe larger volumes of the universe and always lead to larger surface densities.

If we make the further assumption that $N(\mu_0, R)$ is separable, and can be expressed as $N(\mu_0)f(R)$, then

$$\Sigma(\mu, \alpha) = \frac{N(\mu_0 = \mu)}{\alpha^4} \int_0^\infty f(R) R^3 dR. \quad (5)$$

For an assumed form of $f(R)$, the fraction of objects with physical scale length R , Equation 5 may be inverted to recover $N(\mu_0)$ from the observed distribution of surface densities and angular scale lengths. However, if $N(\mu_0, R)$ is not separable, than the integral in equation 5 is not independent of μ_0 and the relative proportion of galaxies in terms of surface density $\Sigma(\mu, \alpha)$ does not reflect the relative proportion of galaxies in real space.

The integral over R diverges unless $f(R)$ falls off more quickly than R^{-3} for large R ; this seems to be the case, as there are no known galaxies to date which have scale lengths larger than 100 kpc. We may uncover some confirmation for the cutoff at large R from the POSS-II survey for LSBs, a diameter-limited sample of LSBs (Schombert et al. 1992) which includes several extremely large galaxies similar to the giant LSB Malin-I (Bothun et al. 1987). HI observations of the “V” subsample of LSBs ($30'' < \theta < 1'$) have a 70% detection rate, and imply a V/V_{max} statistic compatible with a uniform redshift distribution. If $\Sigma(\mathcal{R})d\mathcal{R}$ is the number of galaxies in a diameter limited sample with physical radii at the isophotal diameter between \mathcal{R} and $\mathcal{R} + d\mathcal{R}$, then the number density of galaxies with physical radii between \mathcal{R} and $\mathcal{R} + d\mathcal{R}$ is

$$N(\mathcal{R}) d\mathcal{R} = 3\alpha_0^3 \frac{\Sigma(\mathcal{R})}{\mathcal{R}^3} \quad (6)$$

where $\alpha_0 \equiv [\alpha_{min}^{-3} - \alpha_{max}^{-3}]^{-1/3}$ and α_{min} and α_{max} are the diameter limits of the survey. The luminosity density is

$$\mathcal{L}(\mathcal{R}) d\mathcal{R} = 3\bar{\Sigma}\alpha_0^3 \frac{\Sigma(\mathcal{R})}{R}, \quad (7)$$

assuming $\bar{\Sigma}$ is the mean surface brightness within \mathcal{R} . These distributions are plotted in Figure 9. Although the completeness and selection biases of the Schombert et al. catalog are poorly understood, the strong drop-off in luminosity density around $\mathcal{R}_{max} = 10$ kpc seems quite robust; including the galaxies that were not detected in HI could push the flat luminosity density out to $\mathcal{R}_{max} = 20$ kpc, but no further. While there are some galaxies with rather large sizes, the evidence suggests that they are neither an important contributor to the number density or to the luminosity density. McGaugh & Bothun (1994) have done follow up observations of roughly a dozen of the galaxies from the POSS-II survey which suggest that the exponential scale length is typically one-quarter to one-half of the isophotal radius. This allows us to estimate the exponential scale length R given the isophotal radius \mathcal{R} .

The Schombert catalog data plotted in Figure 9(b) suggests that $f(R)$ is best described by a power law

$$f(R) = f_0 R^{-2} \quad (8)$$

between $R_{min} = 0.2$ kpc and $R_{max} = 5$ kpc, where here R is the radius of the galaxy at the limiting isophote of the POSS-II survey.

A. References

Allen, R. J., & Shu, F. H. 1979, *Ap. J.*, 227, 67.

Bardeen, J. M., Bond, J. R., Kaiser, N., & Szalay, A. S. 1986, *Ap. J.*, 304, 15.

Bothun, G. D., Impey, C. D., & Malin, D. F. 1991, *Ap. J.*, 376, 404.

Bothun, G. D., Impey, C. D., Malin, D. F., & Mould, J. 1987, *A. J.*, 94, 23.

Bothun, G. D., Schombert, J. M., Impey, C. D., Sprayberry, D., McGaugh, S. S. 1993, *A. J.*, 106, 530.

Caldwell, N., Armandroff, T. E., Seitzer, P., & Da Costa, G. S. 1992, *A. J.*, 103, 840.

Catelan, P. & Theuns, T. 1996, to appear in *M.N.R.A.S.*, .

Dalcanton, J. J. 1996, *Ap. J.*, 466, 92.

Dalcanton, J. J., Spergel, D. N., & Summers, F. J. 1997, *Ap. J.*, 482, in press.

Davies, J. I., Disney, M. J., Phillipps, S., Boyle, B. J., & Couch, W. J. 1994, *M.N.R.A.S.*, 269, 349.

Davies, J. I., Phillipps, S., Cawson, M., Disney, M., & Kibblewhite, E. 1988, *M.N.R.A.S.*, 232, 239.

de Blok, W. J. G., van der Hulst, J. M., & Bothun, G. D. 1995, *M.N.R.A.S.*, 274, 235.

de Jong, R. S. 1996, *Astr. Ap.*, , in press.

de Jong, R. S., & van der Kruit, P. C. 1994, *Astr. Ap. Suppl.*, 106, 451.

Disney, M. J. 1976, *Nature*, 263, 573.

Disney, M., & Phillipps, S. 1983, *M.N.R.A.S.*, 205, 1253.

Driver, S. P. & Phillipps, S. 1996, *Ap. J.*, 469, 529.

Ellis, R. S., Colless, M., Broadhurst, T., Heyl, J., & Glazebrook, K. 1996, *M.N.R.A.S.*, 280, 235.

Freeman, K. 1970, *Ap. J.*, 160, 811.

Gunn, J. E., *et al.* 1987, *Opt. Eng.*, 26, 779.

Impey, C., Bothun, G., & Malin D. 1988, *Ap. J.*, 330, 634.

Impey, C., Sprayberry, D., Irwin, M., & Bothun, G. 1996, *Ap. J. Suppl.*, 105, 209.

Irwin, M. J., Davies J. I., Disney, M. J., & Phillips, S. 1990, *M.N.R.A.S.*, 245, 289.

Jarvis, J. F., & Tyson, J. A., 1981, *A. J.*, 86, 476.

Knezek, P. 1993, Ph.D. Thesis, University of Massachusetts.

Landolt, A. 1992, *A. J.*, 104, 340.

Loveday, J., Peterson, B. A., Eftathiou, G., & Maddox, S. J. 1992, *Ap. J.*, 390, 338.

Marzke, R. O., Geller, M. J., Huchra, J. P., & Corwin, H. G. 1994, *A. J.*, 108, 437.

McGaugh, S. S., & Bothun, G. D. 1994, *A. J.*, 107, 530.

McGaugh, S. S. 1994, *Ap. J.*, 426, 135.

McGaugh, S. S. 1994, *Nature*, 367, 538.

McGaugh, S. S. 1995, in New Light on Galaxy Evolution, IAU Symp. 171, ed. R. Bender & R. Davies (Kluwer), in press.

McGaugh, S. S. 1996, *M.N.R.A.S.*, 280, 337.

Mo, H. J., McGaugh, S. S., & Bothun, G. D. 1994, *M.N.R.A.S.*, 267, 129.

Nilson, P. 1973, Uppsala Astr. Obs. Ann., 6, 1.

Peterson, B. A., Ellis, R. S., Efstathiou, G., Shanks, T., Bean, A. K., Fong, R., & Zen-Long, Z. 1986, *M.N.R.A.S.*, 221, 233

Phillipps, S., Davies, J. I., & Disney, M. J. 1990, *M.N.R.A.S.*, 242, 235.

Postman, M., Lubin, L. M., Gunn, J. E., Oke, J. B., Schneider, D. P., Hoessel, J. G., & Christensen, J. A. 1996, *A. J.*, 111, 615.

Roukema, B. F., & Peterson, B. A. *Astr. Ap. Suppl.*, 109, 511.

Sandage, A., & Binggeli, B. 1984, *A. J.*, 89, 919.

Schneider, D. P., Schmidt, M., & Gunn, J. E. 1994, *A. J.*, 107, 1245.

Schombert, J. M., & Bothun, G. D. 1988, *A. J.*, 95, 1389.

Schombert, J. M., Bothun, G. D., Schneider, S. E., & McGaugh, S. S. 1992, *A. J.*, 103, 1107

Schwartzenberg, J. M., Phillips, S., Smith, R. M., Couch, W. J., & Boyle, B. J. 1995, *M.N.R.A.S.*, 275, 121.

Sprayberry, D., Impey, C., & Irwin, M. J. 1996, *Ap. J.*, 463, 535.

Sprayberry, D., Impey, C., Irwin, M. J. & Bothun, G. D. 1997, *Ap. J.*, 481, in press.

Turner, J. A., Phillips, S., Davies, J. I., & Disney, M. J. 1993, *M.N.R.A.S.*, 261, 39.

Valdes, F. 1982, *S.P.I.E.*, 331, 465.

Table 1. LSB Subsample

object	ID	RA (1950.0)	Dec (1950.0)	$\mu_0(V)$ mag/ \square''	α ($''$)	h h_{50}^{-1} kpc	M_V	cz km/s	Spectral Features
PG 0849+4748	R-27-1	8 49 28.4	+47 48 37	23.1	4.3	3.6	-18.3	8809	$H\beta, O[III], H\alpha$
PG 0847+4747	R-26-1	8 47 44.9	+47 47 48	23.2	2.6	-	-	-	
PG 1521+4632	M-232-1	15 21 32.4	+46 32 58	23.6	3.2	1.7	-16.1	5600:	break?
PG 1136+4750	Q-129-2	11 36 46.1	+47 50 41	23.7	4.5	1.9	-16.2	4270	$H\beta, O[III], H\alpha$
PG 0914+4744	Q-42-1	9 14 24.5	+47 44 48	23.9	6.1	3.0	-17.1	5400	break, $H\beta$?
PG 1133+4755	R-127-1	11 33 35.4	+47 55 26	24.7	6.9	3.6	-16.7	5250	break
PG 1327+4637	M-161-1	13 27 46.2	+46 37 47	24.8	6.2	3.5	-16.5	5600	break

Fig. 1.— (a) Classification of artificial LSBs as a function of exponential disk profile α and central surface brightness μ_0 . The symbols represent the classification assigned to each artificial galaxy: LSB (*large triangle*), possible LSB (*small triangle*), other classification(s) (*asterix*), no classification (*open circle*). The solid lines are lines of constant signal-to-noise (i.e. varying values of μ_{zp}).

(b) Classification efficiency vs μ_{zp} . The fraction of LSBs from Figure 1[a] which were correctly identified as LSBs, as a function of μ_{zp} (solid lines in Figure 1[a]). The dotted line is the fit given in equation 1.

Fig. 2.— Images of the LSBs in the final subsample. Each image consists of three panels taken from different stages of processing, centered on the position of the candidate and adjusted to a common angular size. The first panel is taken from the data before cleaning. The second panel is taken from the data after cleaning, flattening, and rebinning by a factor of two. The third panel is the smoothed image used for detection. Because of cleaning, high surface brightness features detectable in the leftmost panel may not be visible in the central cleaned image, although there is sufficient diffuse emission which is uncleaned for the galaxy to be detected in the smoothed image.

Fig. 3.— Radial surface brightness profiles for the LSBs in the final subsample. Dashed lines are fits of exponential surface brightness profiles to the measured intensity. The error bars include the photometric uncertainty at each radius, as well as the uncertainty in the sky subtraction.

Fig. 4.— (a) Detection efficiency of artificial LSBs as a function of exponential disk profile α and central surface brightness μ_0 . The contours are lines of constant detection efficiency, separated by 0.1. The locations of the artificial galaxies which were successfully detected in Monte Carlo simulations are plotted as small \times 's. The triangles are LSB candidates with $\mu_0 > 23 \text{ mag/arcsec}^2$ in V . The dashed line is the region of 100% classification efficiency, and the dotted line is where the classification efficiency approaches zero.

(b) Binned detection efficiency as a function of exponential disk profile α , for μ_0 between 23 and $25.5 \text{ mag/arcsec}^2$ in V , in steps of 0.5; the symbol size increases with increasing surface brightness. The solid line is the gaussian approximation given in equation 2.

Fig. 5.— Spectra of individual LSBs (dark lines, lower spectrum), compared with the template LSB spectra which were used for cross-correlation (light lines, upper spectrum) and which were generated by averaging the spectra from all other LSBs, excluding R-26-1. Spectra have been shifted to their rest-wavelengths; we have shifted the uncertain R-26-1 spectrum by $cv = 17200 \text{ km/s}$. For comparison, the final panel compares one composite LSB spectra with a K1III giant observed with the same instrumental arrangement after a wavelength dependent flux correction has been applied. All spectra have been smoothed with a 3 pixel boxcar filter, except R-26-1, M-232-1, and M-161-1, which were smoothed with a 5 pixel boxcar filter. The coadded LSB spectra have been given an arbitrary vertical offset to facilitate comparison. The [OII] line is broadened, due to an inability to maintain the focus the spectrograph in the UV. Obvious sky subtraction errors at bright sky lines have been interpolated over, for clarity of presentation.

Fig. 6.— Space-Redshift diagram for the LSBs in the final subsample (*triangles*, excluding R-26-1) and normal galaxies (*circles*) taken from the ZCAT redshift catalog. The normal galaxies are taken from 1 deg wide strips in declination, spanning the range of right ascensions mapped by the survey. At 5500 km/s , the width of the 1 deg strip is $1.9 h_{50}^{-1} \text{ Mpc}$.

Fig. 7.— The integrated number density of LSB galaxies with $\mu_0 > 23 \text{ mag/arcsec}^2$ in V . The dashed lines encompass the 90% confidence interval. The arrows are drawn at the integrated number density of normal galaxies, as cataloged by the DARS survey (Peterson et al. 1986), the Stromlo-APM survey (APM; Loveday et al. 1992), and the AutoFib survey (AF; Ellis et al. 1996). The range of integration was restricted to either

the same scale lengths (“same α ”; right axis) or same absolute magnitudes (“same M”; left axis) as the LSBs in the survey.

Fig. 8.— Similar to Figure 7, except the integrated luminosity density of LSB galaxies with $\mu_0 > 23 \text{ mag/arcsec}^2$ in V is plotted, in units of $L_*h_{50}Mpc^{-3}$, chosen to correspond to $M_{b_j} = -19.5$. The dashed lines encompass the 90% confidence interval. The arrows are drawn at the luminosity density of normal galaxies, as cataloged by the DARS survey (Peterson et al. 1986), the Stromlo-APM survey (APM; Loveday et al. 1992), and the AutoFib survey (AF; Ellis et al. 1996). The range of integration was restricted to either the same scale lengths (“same α ”; right axis) or same absolute magnitudes (“same M”; left axis) as the LSBs in the survey.

Fig. 9.— The distribution of radii for the Schombert et al. (1992) “V” catalog of LSBs, and the implied relative number and luminosity density of LSBs as a function of physical size. The angular diameters and distances for the LSBs have been converted to physical radii, making no correction for the dependence of angular size on surface brightness. (a) The number of objects per $0.2 \log(R/\text{kpc})$ in the catalog. There are 71 LSBs in the distribution. There are an additional 29 galaxies which were observed in HI but not detected. The dotted lines are drawn for power-law slopes of 0.5, 1, and 1.5. The distribution is consistent with slopes of 1 and 1.5, but not 0.5. (b) The relative number density of galaxies per $0.2 \log(R/\text{kpc})$, calculated by correcting the distribution in (a) for the size of the volume in which the LSBs could have been identified, given the diameter limits of the survey and the physical sizes of the galaxies at their diameter limits (see eqn. 6). The dotted lines are drawn for power-law slopes of -1.5, -2, and -2.5. (c) The relative luminosity density of LSBs per $0.2 \log(R/\text{kpc})$, calculated from (b) assuming a constant mean surface brightness within R , so that luminosity is proportional to R^2 (see eqn. 6). The luminosity density is relatively flat between 0.5 kpc and 10 kpc, but drops precipitously at larger sizes. The LSBs in the “V” catalog do not have well determined selection criteria; as such, these plots should not be taken as definitive measurements, but as rough estimates. They have central surface brightnesses $< 24 B \text{ mag/arcsec}^2$, brighter than almost all of the candidates in our survey.

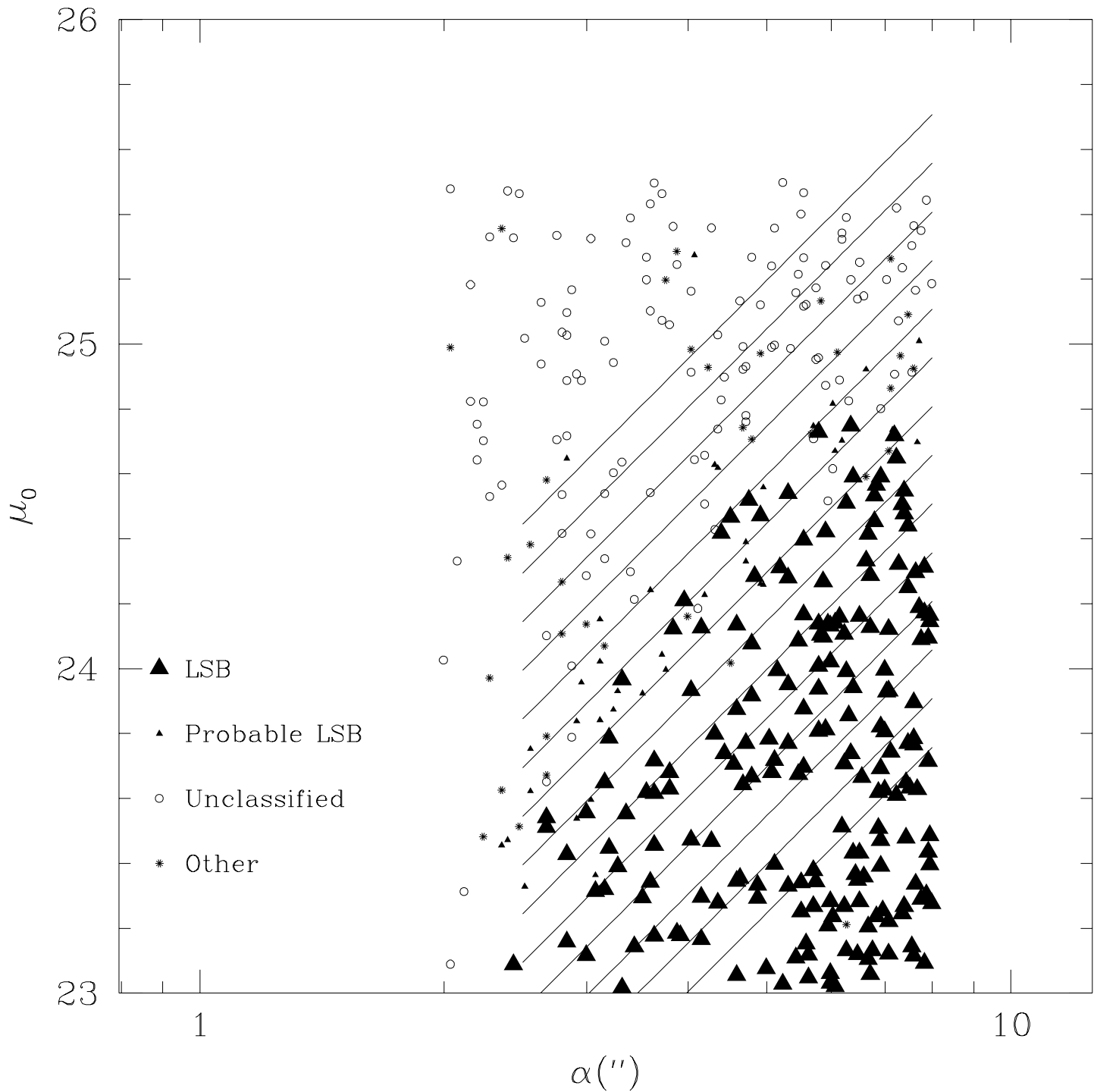


FIGURE 1[A]

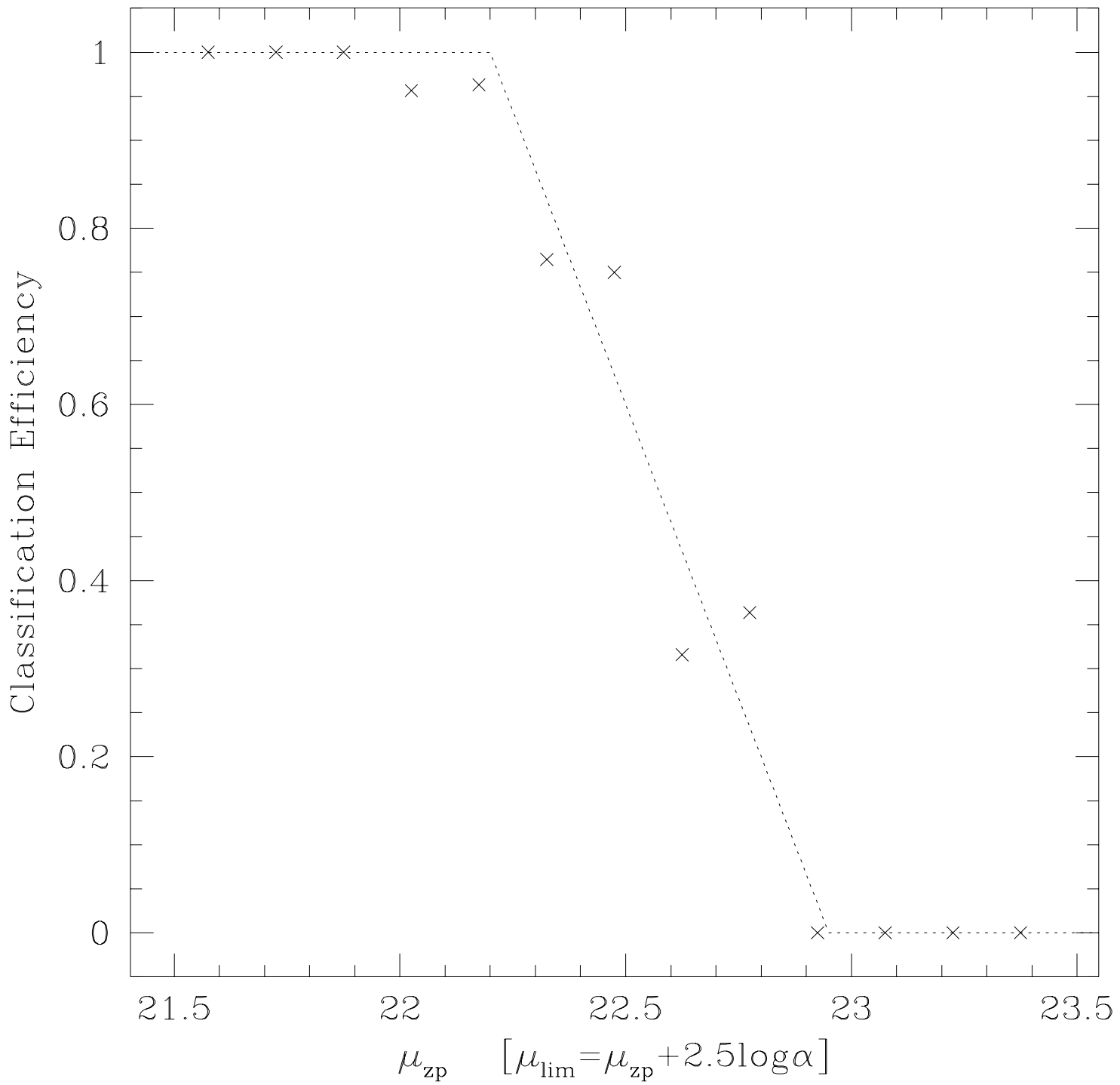


FIGURE 1[B]

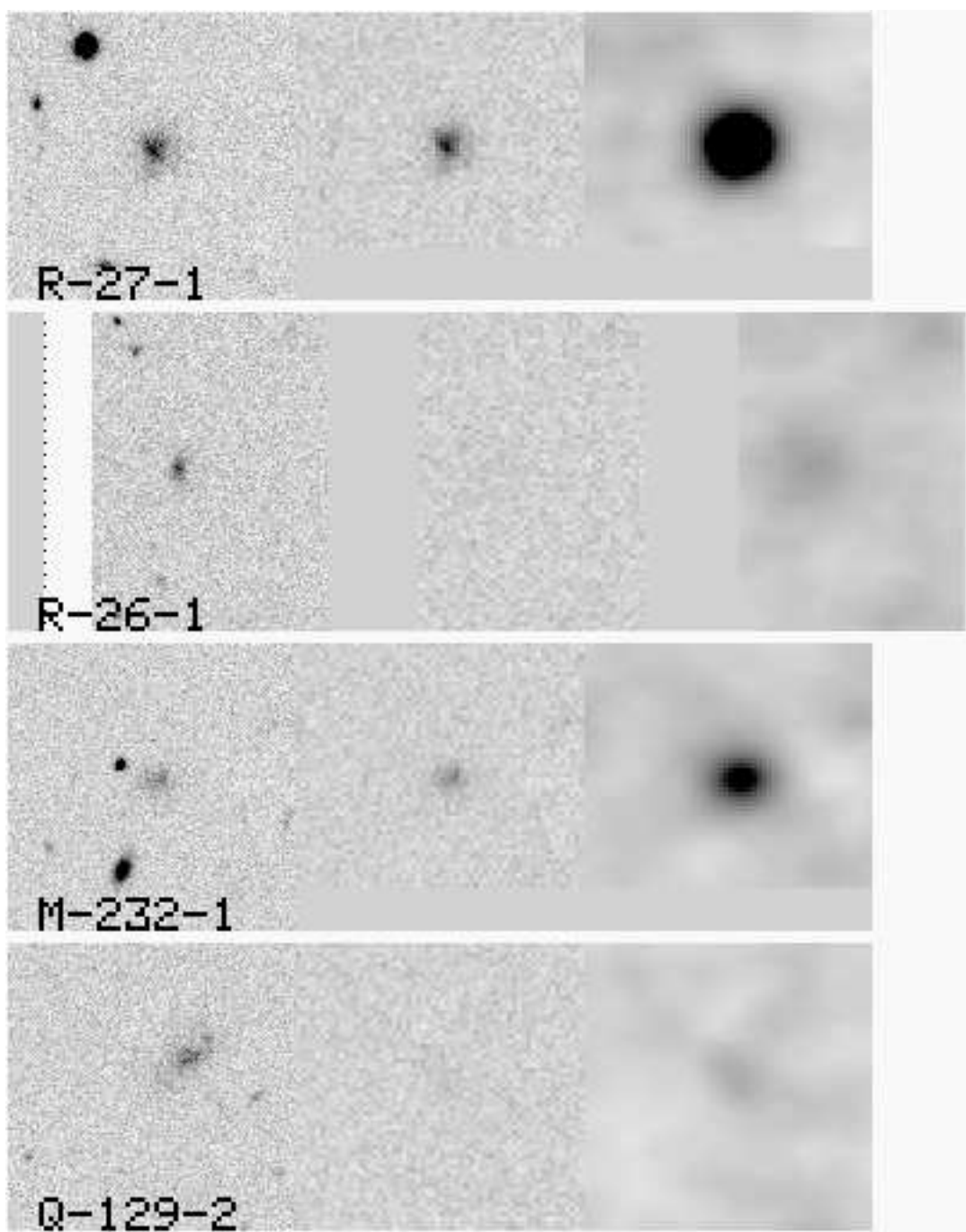


FIGURE 2

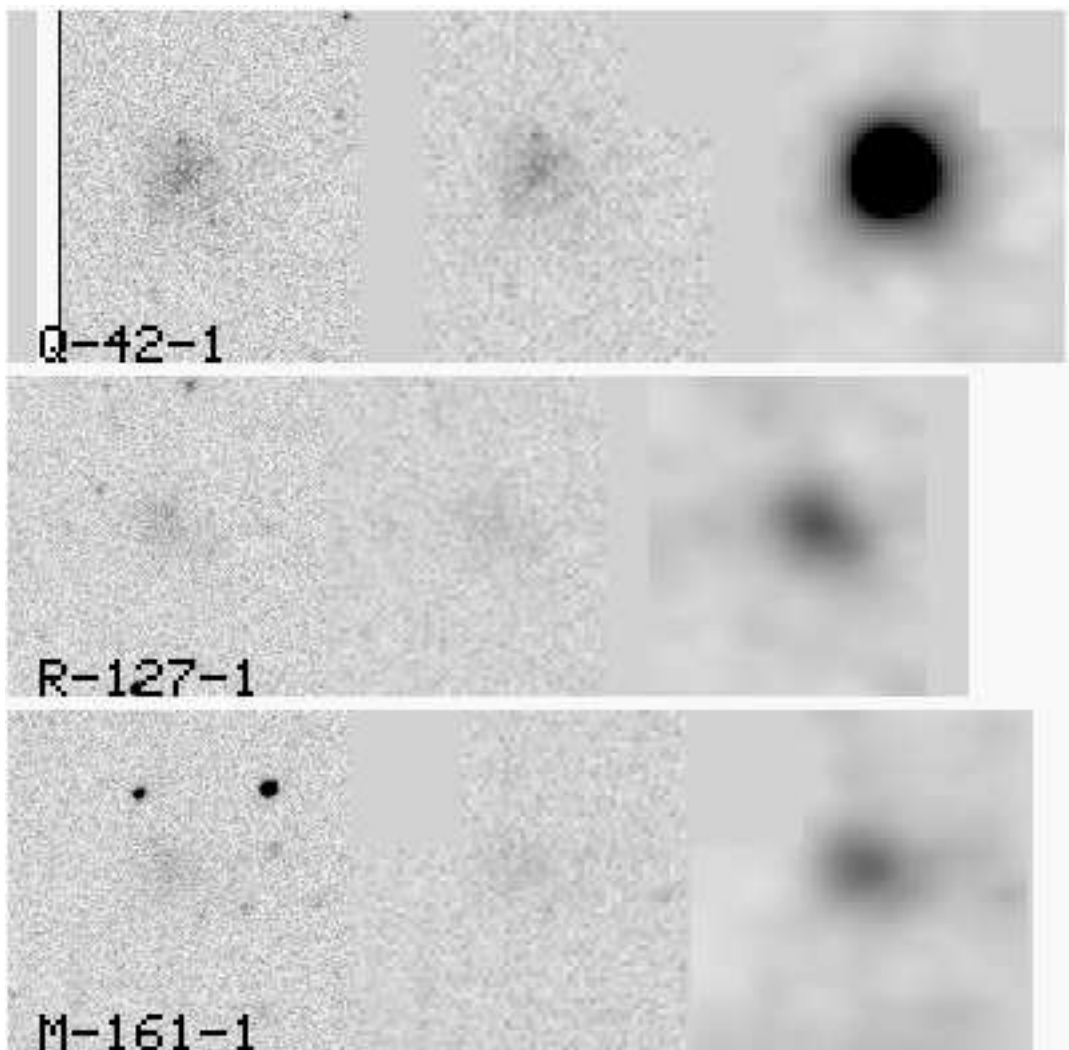


FIGURE 2 (CONTINUED)

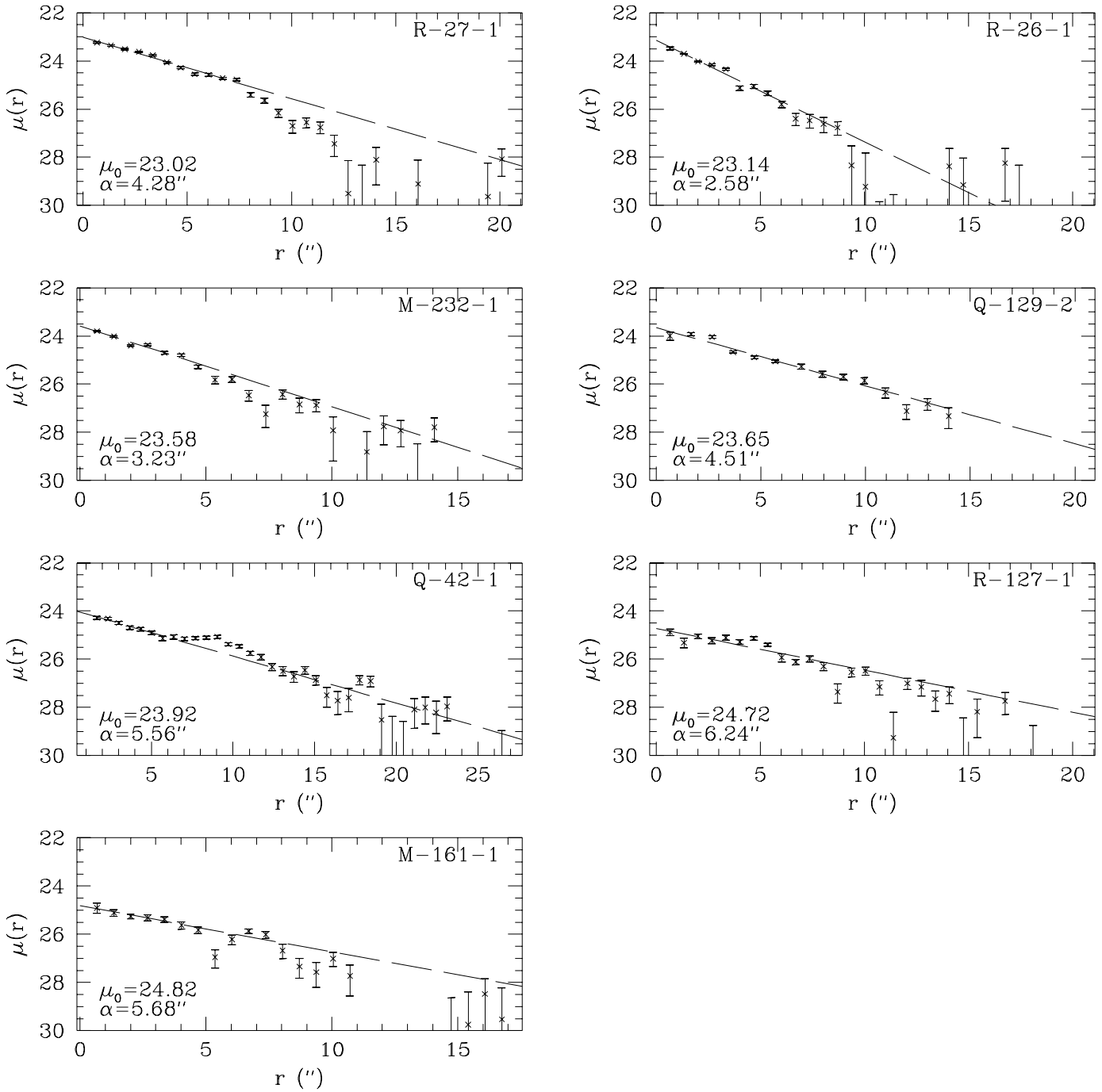


FIGURE 3

Relative Detection Efficiency: $\epsilon=0-0.6$ $\Delta\epsilon=0.02$

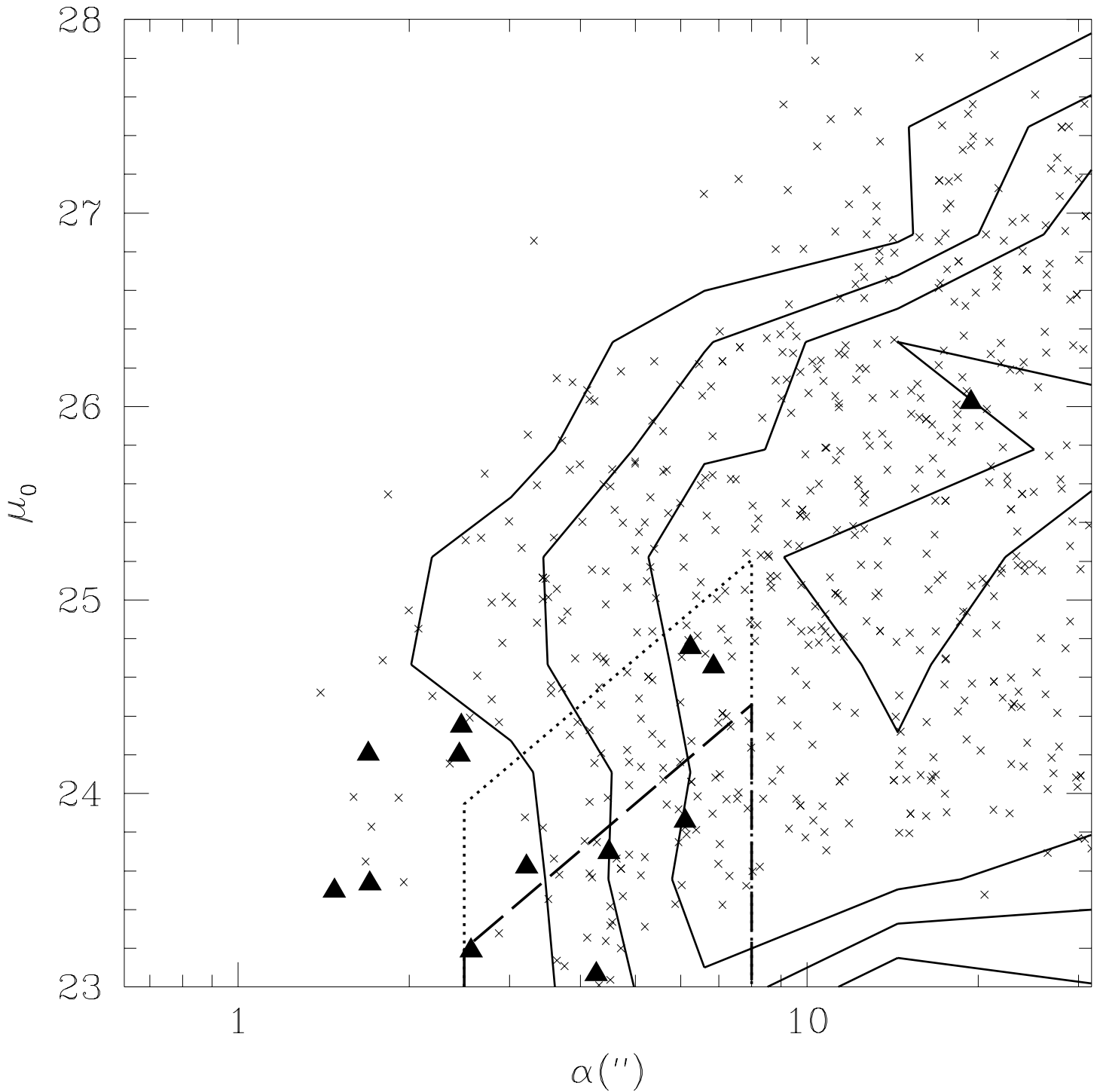


FIGURE 4[A]

$$\epsilon = 0.255049 \exp[-\lg^2(\alpha/6.3'')/0.55]$$

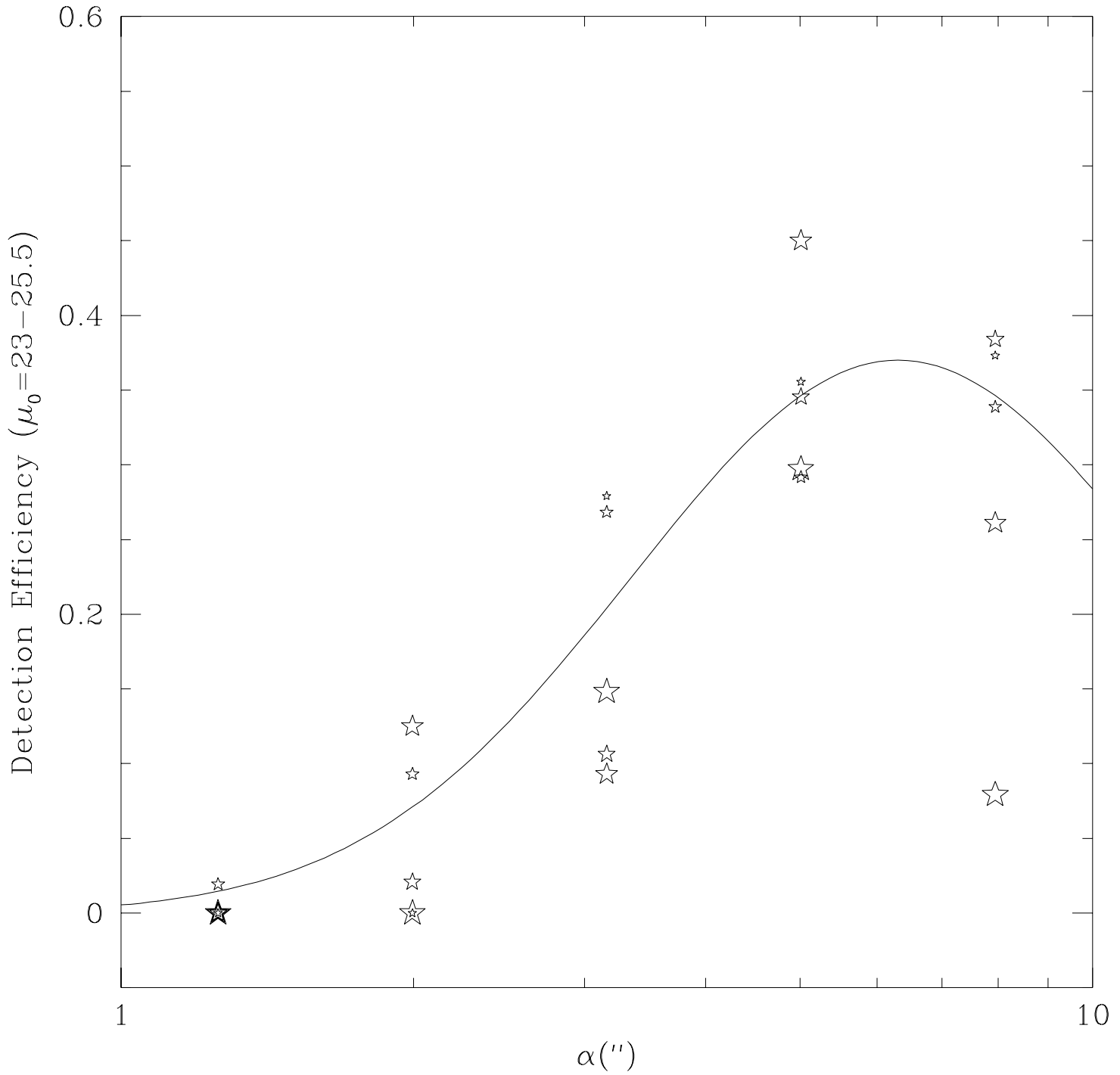
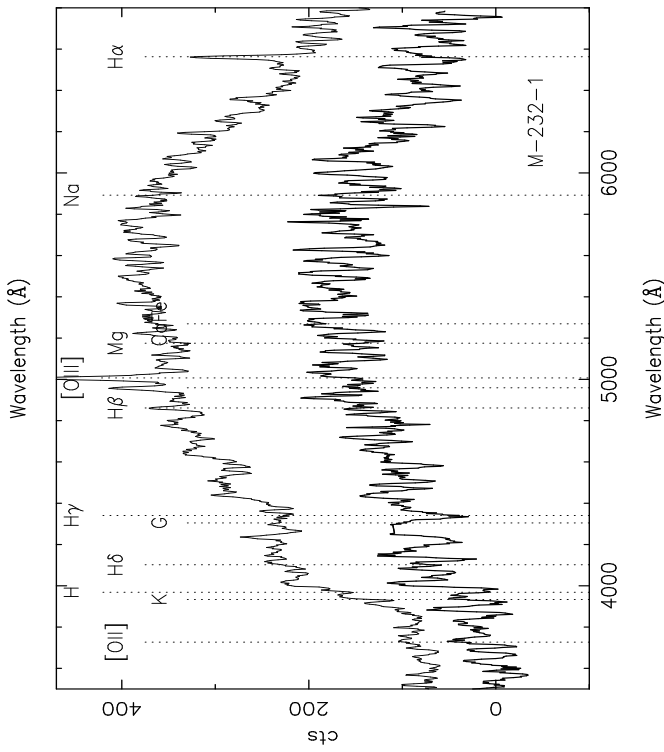
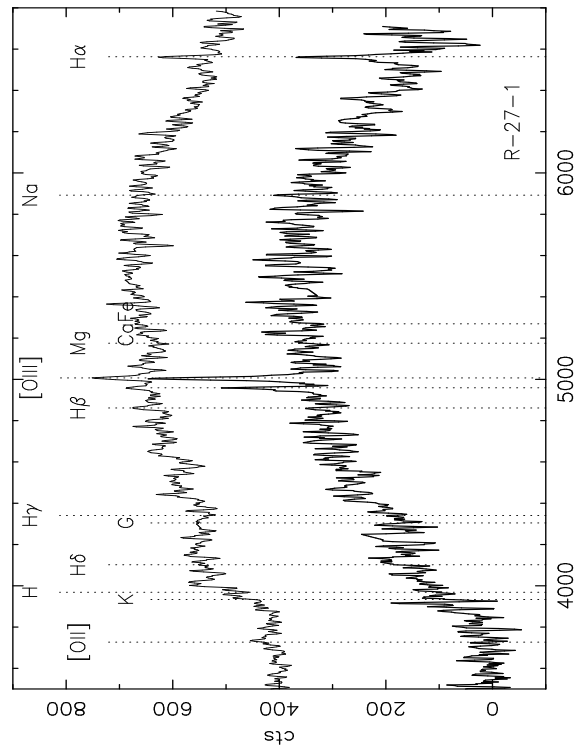
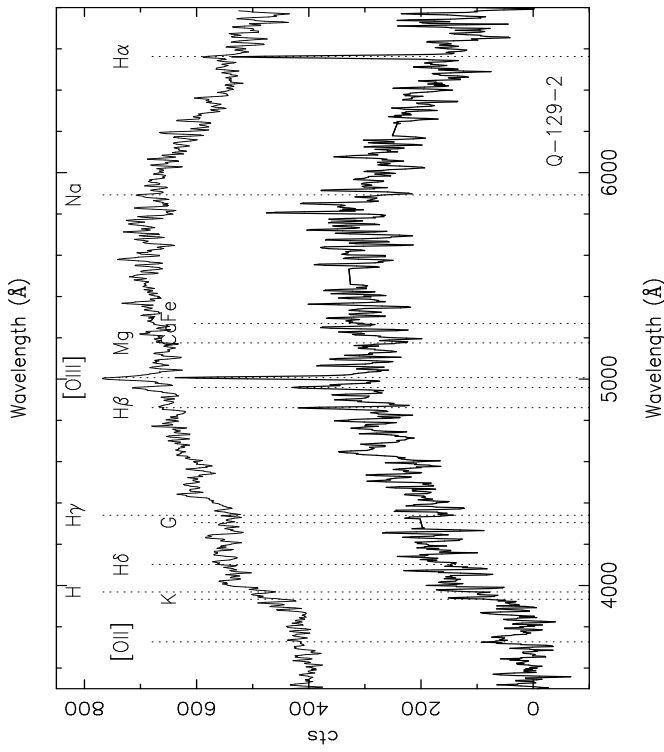
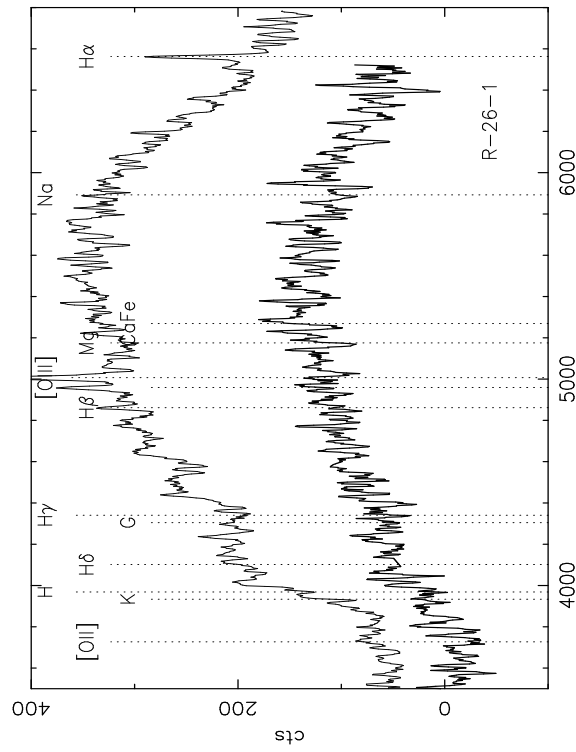
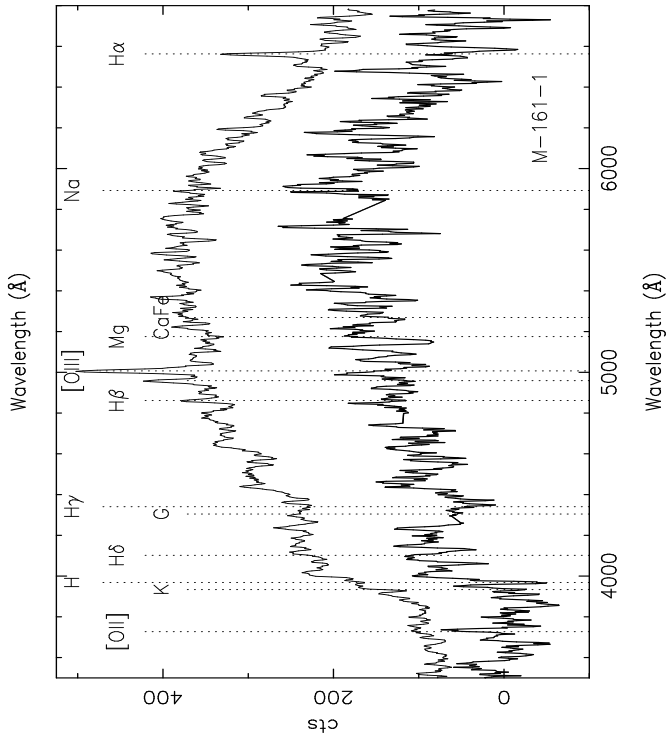
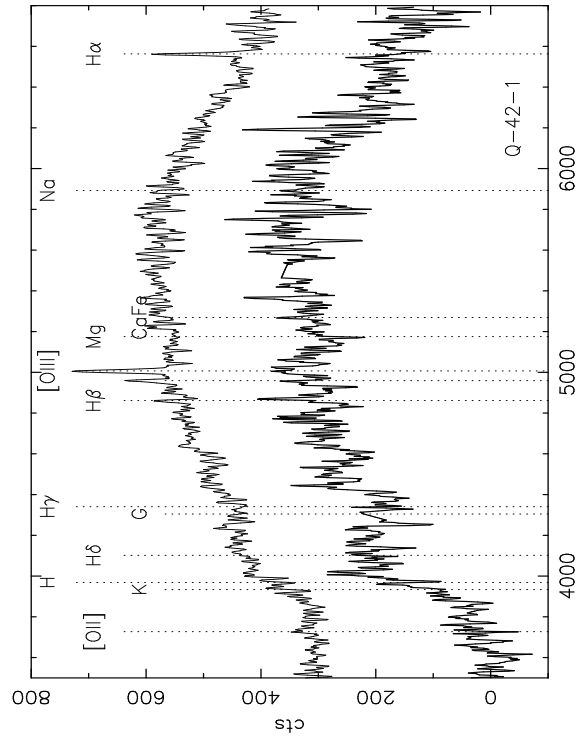
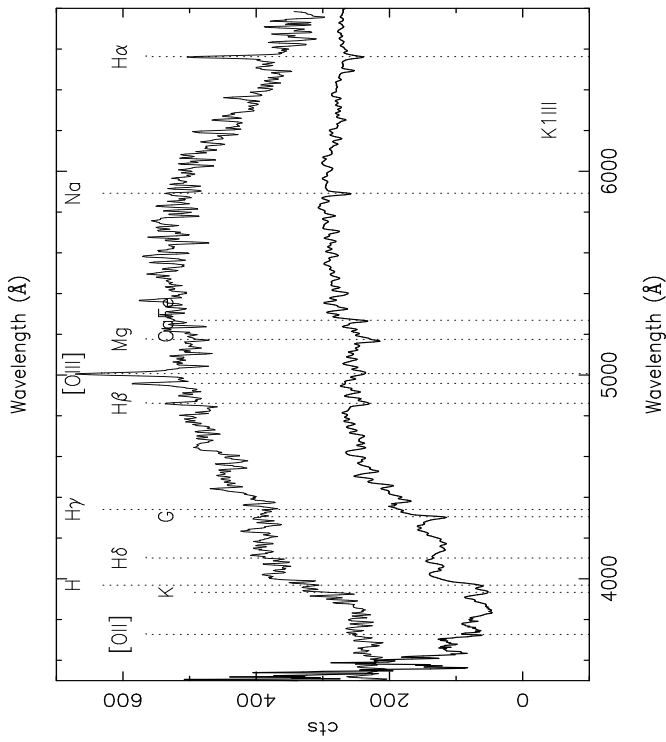
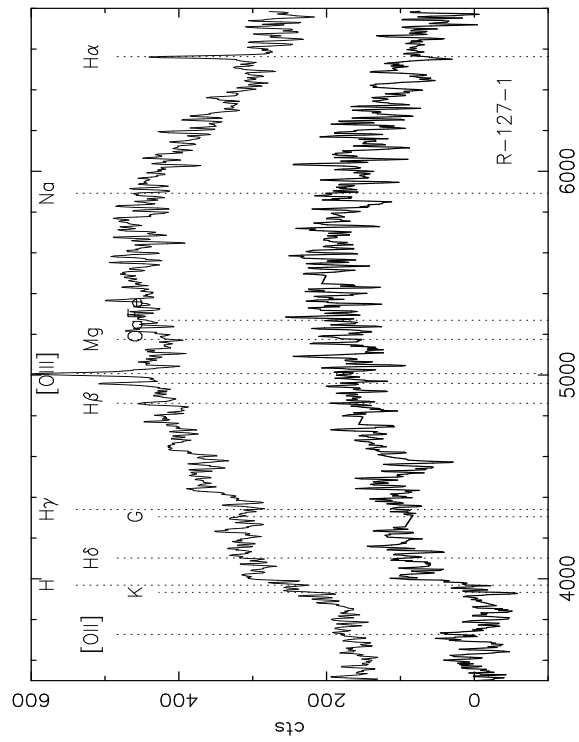


FIGURE 4[B]





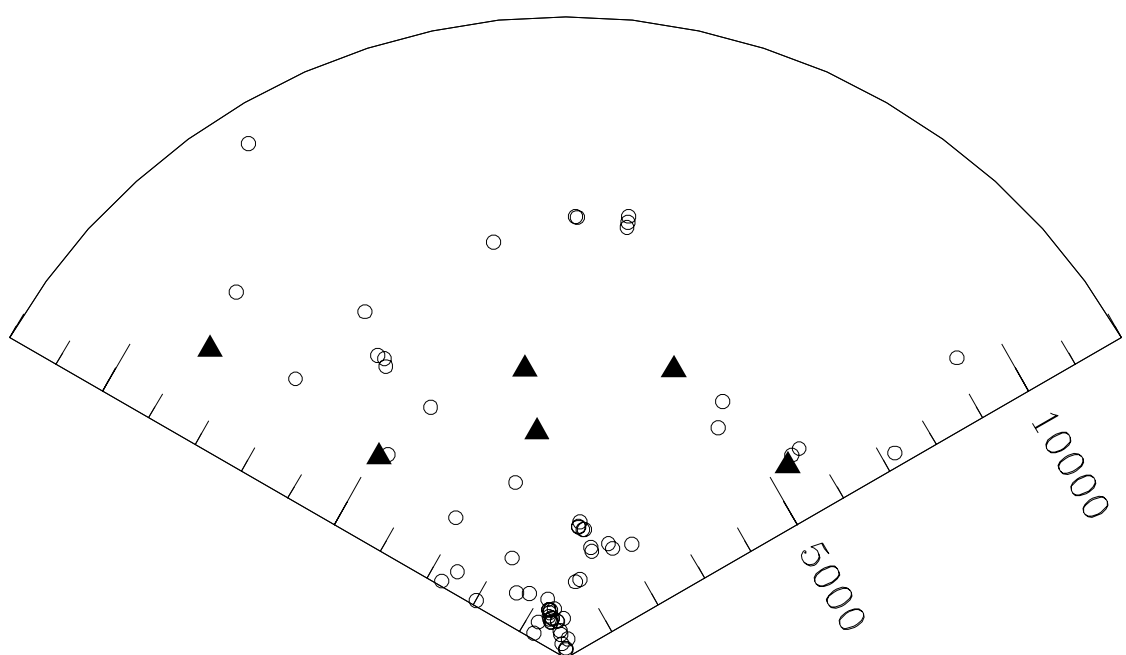


FIGURE 6

Dashed Lines Contain 90% Confidence

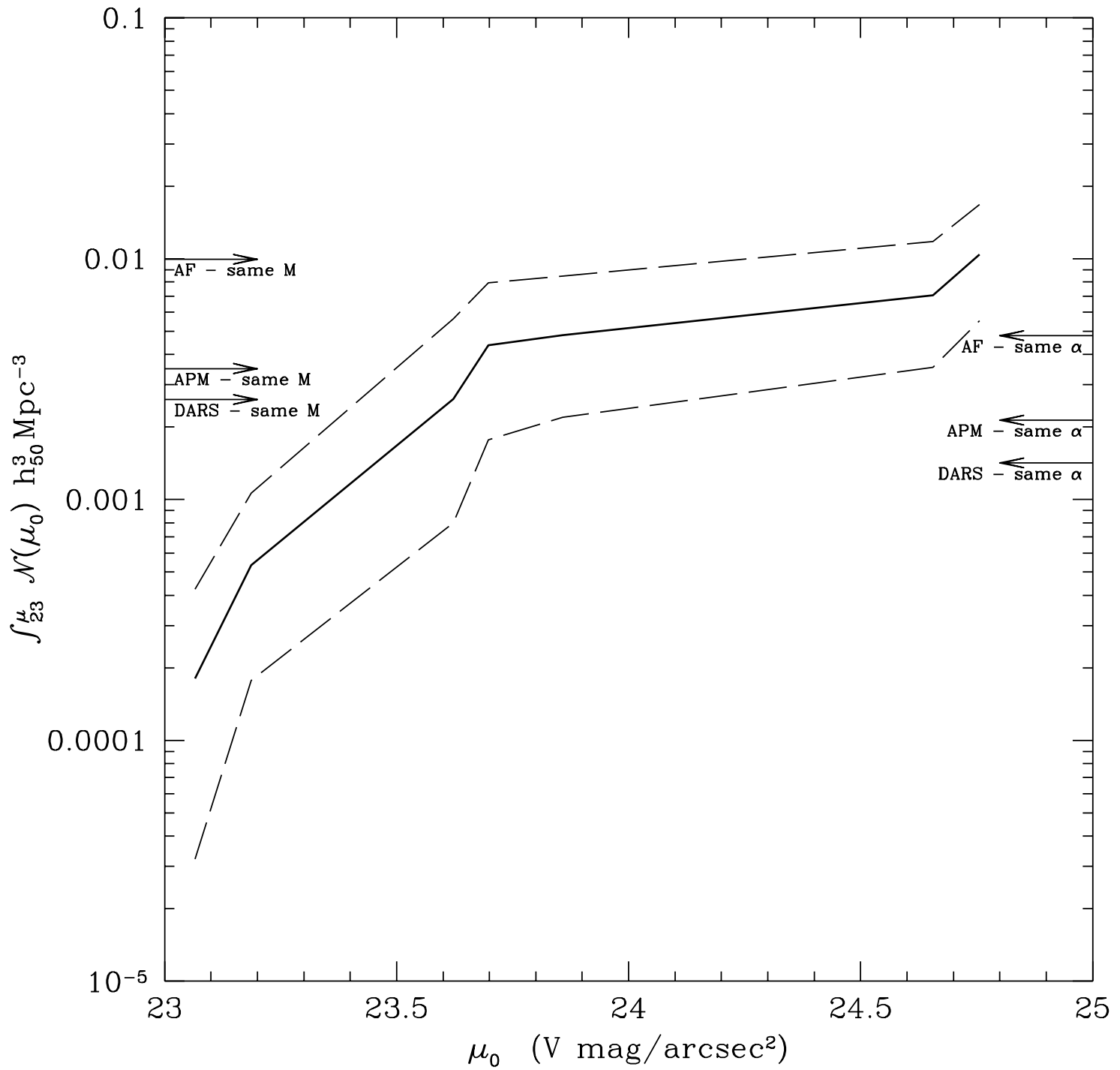


FIGURE 7

Dashed Lines Contain 90% Confidence

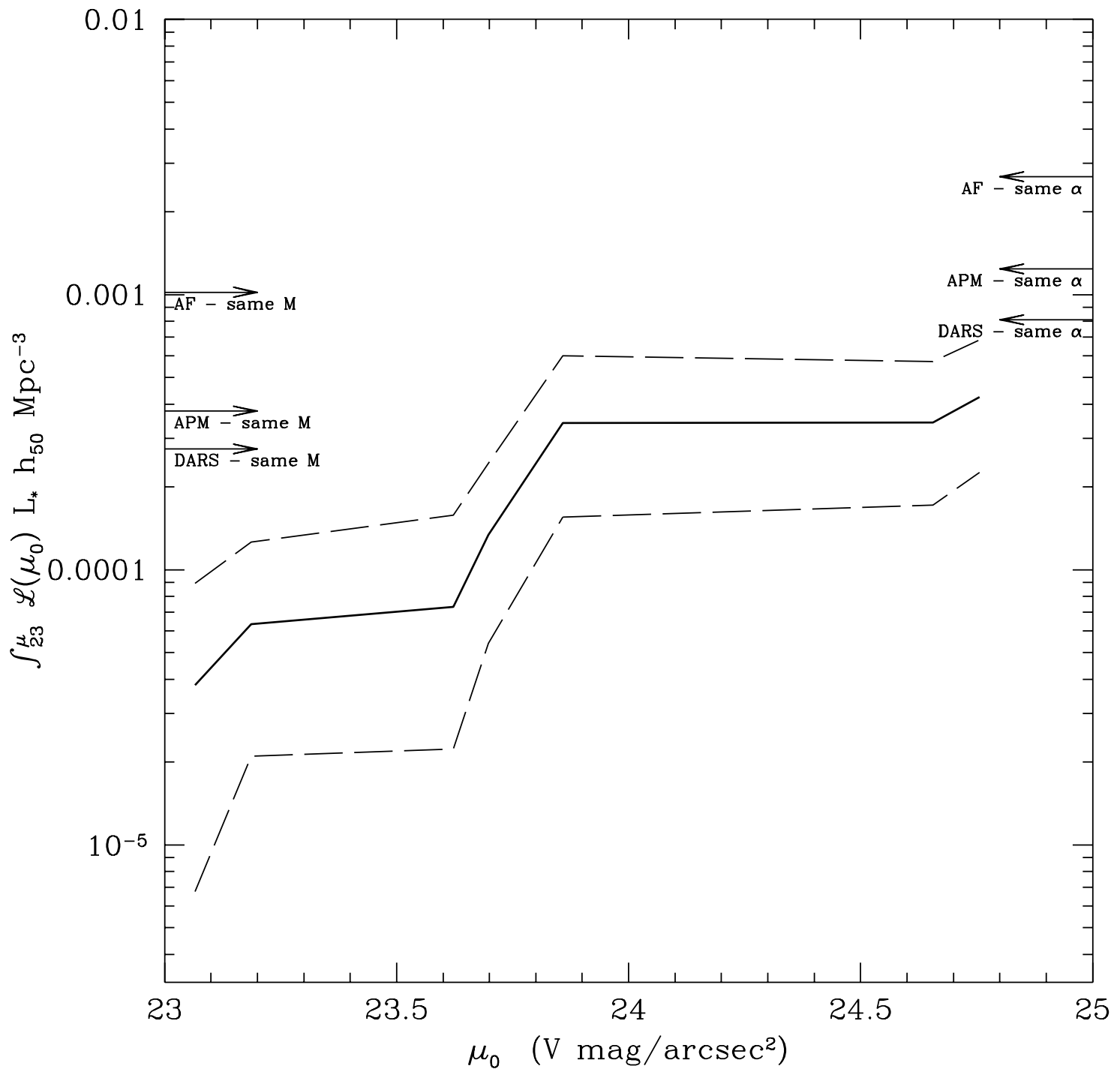


FIGURE 8

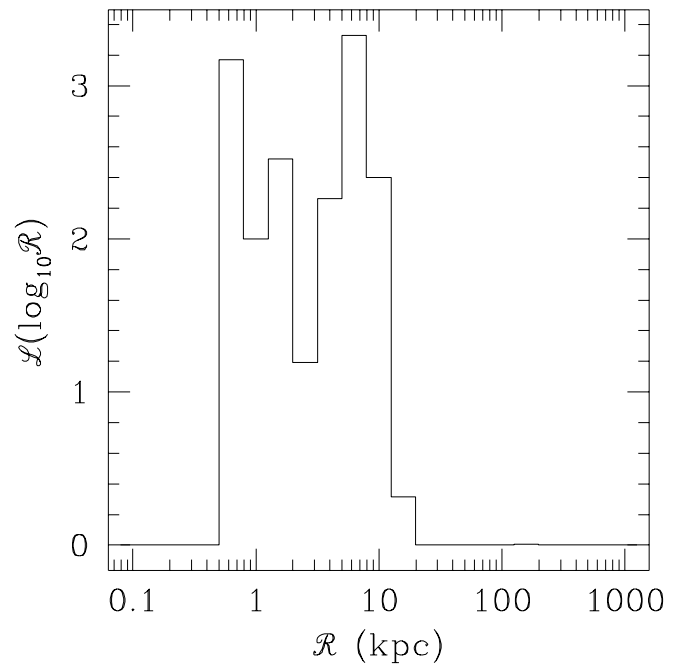
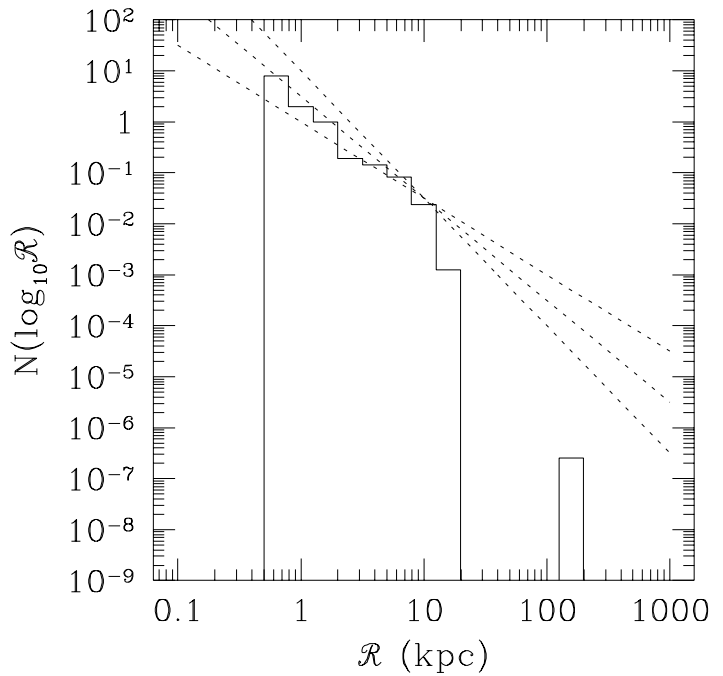
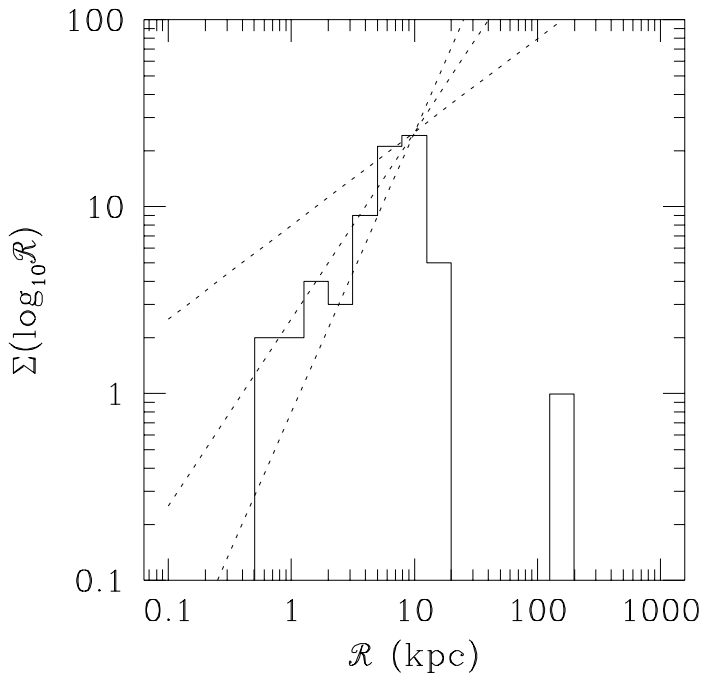


FIGURE 9